

# Relativistic EELS scattering cross-sections for microanalysis based on Dirac solutions

Zezhong Zhang<sup>a,b,c</sup>, Ivan Lobato<sup>d</sup>, Hamish Brown<sup>e</sup>, Dirk Lamoen<sup>a,b</sup>, Daen Jannis<sup>a,b</sup>, Johan Verbeeck<sup>a,b</sup>, Sandra Van Aert<sup>a,b</sup>, Peter D. Nellist<sup>c</sup>

<sup>a</sup> *Electron Microscopy for Materials Research (EMAT), University of Antwerp, Groenenborgerlaan 171, 2020 Antwerp, Belgium*

<sup>b</sup> *NANOLab Center of Excellence, University of Antwerp, Groenenborgerlaan 171, 2020 Antwerp, Belgium*

<sup>c</sup> *Department of Materials, University of Oxford, 16 Parks Road, Oxford OX1 3PH, United Kingdom*

<sup>d</sup> *Rosalind Franklin Institute, Harwell Research Campus, Oxfordshire OX11 0FA, United Kingdom*

<sup>e</sup> *Ian Holmes Imaging Centre, Bio21 Molecular Science and Biotechnology Institute, University of Melbourne, Victoria, Australia*

---

## Abstract

The rich information of electron energy-loss spectroscopy (EELS) comes from the complex inelastic scattering process whereby fast electrons transfer energy and momentum to atoms, exciting bound electrons from their ground states to higher unoccupied states. To quantify EELS, the common practice is to compare the cross-sections integrated within an energy window or fit the observed spectrum with theoretical differential cross-sections calculated from a generalized oscillator strength (GOS) database with experimental parameters. The previous Hartree-Fock-based and DFT-based GOS are calculated from Schrödinger's solution of atomic orbitals, which does not include the full relativistic effects. Here, we attempt to go beyond the limitations of the Schrödinger solution in the GOS tabulation by including the full relativistic effects using the Dirac equation within the local density approximation, which is particularly important for core-shell electrons of heavy elements with strong spin-orbit coupling. This has been done for all elements in the periodic table (up to  $Z = 118$ ) for all possible excitation edges using modern computing capabilities and parallelization algorithms. The relativistic effects of fast incoming electrons were included to

calculate cross-sections that are specific to the acceleration voltage. We make these tabulated GOS available under an open-source license to the benefit of both academic users as well as allowing integration into commercial solutions.

*Keywords:* Electron energy loss spectroscopy (EELS), Generalized oscillator strength (GOS), Ionization, Inelastic electron scattering

---

## 1. Introduction

Electron energy-loss spectroscopy (EELS) involves analyzing the energy loss distribution of electrons after their interaction with a specimen. With the underlying inelastic electron scattering event, the fast-moving incident electron transfers part of its energy and momentum by exciting the atomic system from its initial quantum ground state to various excited final states [1]. Since these transitions are characteristic of the type of elements and their local electronic structure, EELS can fingerprint the composition and bonding of the specimen. Thanks to advances in instrumentation such as aberration correction [2], monochromation [3, 4] and more recently direct electron cameras [5, 6], EELS can now be performed with high energy resolution (up to meV) and spatial resolution (up to Å). Recognized as a powerful analytical tool for site-specific materials characterization [7, 8], there is a general interest in the accurate and precise quantification of EELS and this therefore necessitates a reliable theoretical model to calculate the inelastic scattering cross-sections, which describes the probability of inelastic scattering events to take place.

To quantify EELS, one has to model the spectra as a superposition of the background signal

---

\*Corresponding author

*Email addresses:* zezhong.zhang@uantwerpen.be (Zezhong Zhang), sandra.vanaert@uantwerpen.be (Sandra Van Aert), peter.nellist@materials.ox.ac.uk (Peter D. Nellist)

and multiple excitation edges with characteristic shapes. The traditional method involves background removal using a power-law extrapolation from the pre-edge region and integration of the edge signal within a certain energy window [9]. For the analysis of fine structures, deconvolution with the low-loss spectrum is performed to remove plural scattering (known as the Fourier-ratio method)[10]. However, this methodology can result in various artifacts during deconvolution and can be very sensitive to the choice of suitable windows for background removal and signal integration [11]. A better approach is to perform a model-based fitting of the observed spectrum with theoretical scattering cross-sections. This has clear benefits: (a) effective separation of overlapping components, (b) consideration of multiple scattering through convolution of the core-loss model with the low-loss spectra instead of deconvolution, and thereby its artifacts, (c) most significantly, the model-based parameter estimation theory grants statistical superiority, resulting in improved accuracy and free from bias [12, 11]. The model-based method is implemented in EELSModel [11] (and its python version pyEELSModel [13]), HyperSpy [14] (the EDX/EELS analysis is recently renamed exspy) and Gatan Microscopy Suite Software<sup>TM</sup>, which are widely used in the EELS community. Continuous efforts have been devoted to improving the model-based EELS, including developing a better background model [15, 16], addressing the correlated noise effects from the camera [17] and incorporating a phenomenological model for the fine structure during signal processing [18]. However, the day-to-day scattering cross-section computation has long relied on the Hartree-Fock (HF) based generalized oscillator strength (GOS) database, which involves some limitations: (1) the HF solutions are not fully relativistic, which can be critical for heavy elements with strong spin-orbit coupling (SOC); (2) not all (though a good coverage) elements and edges are included in the database; (3) the energy-momentum space is limited and

sampling is not fine enough for accurate cross-section calculations; (4) the database is under a commercial license limiting its use in community-driven development.

Theoretical core-shell cross-sections are computed based on a set of experimental parameters (such as acceleration voltage, convergence angle, EELS collection angle, etc) and a GOS database, which couples the atomic physics with electron scattering. The name "generalized oscillator strength" comes from the extension of the "oscillator strength", which describes the probability of absorption or emission of electromagnetic radiation caused by the electron orbital transitions for an atom or molecule [19]. Indeed the precise analysis of atomic light spectra, tracing back to the starting point of quantum mechanics, lays the foundation of atomic physics. The transition probability can be calculated using Fermi's golden rule, which states that the transition probability is proportional to the strength of the coupling between the initial and final states under weak perturbation (first Born approximation). Interestingly, the idea was first formulated by Dirac in 1927 [20], just a year before the publication of the Dirac equation [21]. On its importance for quantum transitions, Fermi referred to it as the "golden rule No. 2" in a university nuclear physics class [22] and thereafter was known as the "Fermi's golden rule". In the context of core-shell electrons, the initial state represents the occupied bound state of a given orbital, while the final states can include unoccupied bound orbitals above the Fermi level or continuum states above the vacuum level after ionization. The local density of unoccupied states highly depends on the valence electron redistribution in the crystal field (known as bonding), leading to complicated energy loss near-edge fine structures (ELNES). In addition, the reflection of outgoing excited electron waves by surrounding atoms will generate the extended energy loss fine structures (EXELFS). In contrast, at a moderate higher energy loss (typically tens of eV above the edge to be free from ELNES and EXELFS), the

perturbation caused by the local environment is much decayed, and the excitation to the continuum states defines the general spectra shape for each edge [10]. Thus, the GOS can be computed for a single isolated atom with final states limited to the continuum state and applied to any material system for the quantification of such an element.

The computation of the theoretical EELS cross-sections dates back to 1932 when Bethe first used the Born approximation to consider the angular-dependent probability of a collision of an electron with matter at relativistic speed using hydrogenic solutions[23]. In the 1950-60s, ionization cross-section studies still often relied on the hydrogenic solutions [24], which describe the intermediate and large energy loss fairly well for K-shells but cannot capture the near-edge behaviors for higher shells. Since the 1970s, improvements were made by McGuire [25], Manson [26] and Scofield [27], who used HF solutions of atomic orbitals to calculate K and L-edges cross-sections of light elements. These HF-GOS efforts were systematically extended to a much broader range of elements and shells by Leapman, Rez and co-workers [28, 29, 30], later becoming the basis for the Gatan GOS database. Many studies in the atomic physics community focused on more accurate computational scattering methods going beyond the plane wave Born approximation [31, 32]. For instance, as the name suggests, the plane wave Born approximation assumes the incoming and outgoing electron to be in the form of a plane wave, which is reliable for the fast electron with kinetic energy well above the ionization threshold, but becomes a problem when the electron is slow and noticeably distorted by the presence of the target atom. In this case, the distorted wave Born approximation method is developed to take the finite influence of atomic potential into account. Meanwhile, much of the attention in the electron microscopy community was devoted to dynamical scattering to explain the complex phenomenon in energy-filtered imaging[33, 34], diffraction

[35], EDS [36] and EELS [37, 38, 39, 40, 41, 42]. In particular, Yoshioka [43] demonstrated that the inelastic scattering and the associated absorption can be treated as an additional transition potential with an imaginary part, forming the basis for the implementations of dynamic inelastic scattering in various algorithms, including Bloch wave [44, 45, 46], multislice [33, 47, 48, 49, 50] and more recently the PRISM algorithm [51]. The fast electron used in mid/high voltage electron microscopes has considerable relativistic effects, which boosts the cross-sections in an anisotropic way across the energy-momentum space. Such relativistic electrodynamics behaviors of the incoming electron beam on the differential scattering cross-sections was first studied by Fano in 1956 [52] and have been later considered in several studies [50, 53, 54, 55, 56] but with orbital wavefunctions based on the Schrödinger solution. In addition, significant interest has emerged in the density functional theory (DFT) community to calculate the fine structure with the density of states explicitly included for EELS [57] and X-ray absorption spectroscopy (XAS) [58], all based on the Schrödinger picture. Given our focus is on the absolute cross-sections for EELS microanalysis, the dynamic scattering effects, and fine structures are beyond the scope of this paper. We noticed a clear pattern in the literature that electron microscopy research typically adheres to the Schrödinger framework, whereas the atomic physics community has long utilized the Dirac framework. Therefore, this paper also aims to bridge the conventions, recognizing that both fields are engaged in the same endeavor.

To go beyond the limitation of the current GOS databases for accurate EELS quantification, here we report the development of an open-source GOS database using the Dirac equation. We want to note that this work at its inception is in parallel with the recent Schrödinger GOS [59, 60], which solved the radial wavefunction with DFT generalized norm-conserving pseudopotential po-

tential [61] (hereafter referred to as the DFT-based GOS). Once we learned about this parallel development, we agreed to adopt the same file standard as GOSH [62] for the convenience of the user. Different from existing Schrödinger-based GOS databases (i.e. HF and DFT), we chose the Dirac equation for its intrinsic incorporation of relativity. This is particularly crucial when the electron approaches the speed of light, especially in heavy elements. In this paper, we will introduce the theoretical background of atomic orbital calculations and inelastic electron scattering. First, we will take the reader through the inelastic scattering from the Schrödinger equation in Sec. 2, followed by a discussion of the relativistic Dirac equation in Sec. 3 to highlight the connections and differences. In the relativistic inelastic scattering theory, we will consider the relativistic effects on the cross-sections due to fast-moving incident electrons. In Sec. 4, we will explain the inclusion of experimental parameters of EELS geometry (i.e. convergence angle and collection angle) in the cross-section calculations. Then, we will present the computational details for GOS database generation in Sec. 5 followed by the results section in Sec. 6. Specifically, Sec. 6.1 will give an overview of the Dirac-based GOS in terms of the energy-momentum sampling compared to existing databases. Then we will explicitly explore the effects of SOC and the contribution of small components which is unique in the Dirac solution. In Sec. 6.2, we will demonstrate the relativistic electrodynamics effects of the incoming fast electron on the cross-sections for typical acceleration voltages and EELS collection angles. In Sec. 6.3, we will compare the Dirac-based GOS with the HF-based GOS and the DFT-based GOS for different elemental edges. Sec. 6.4 will briefly demonstrate how to use the Dirac-based GOS database for EELS quantification. Finally, we will conclude the paper in Sec. 7 with a summary and outlook for future development.

## 2. Theory: non-relativistic atomic orbitals and inelastic electron scattering

In this section, we provide an overview of the Schrödinger equation for atomic orbitals and inelastic electron scattering. For a comprehensive treatment of this topic, readers are referred to Cowan's book on atomic spectroscopy [63], here we only briefly outline the key equations for calculations.

### 2.1. Schrödinger equation for atomic orbitals

In non-relativistic quantum mechanics, the Schrödinger Hamiltonian  $\hat{H}_S$  consists of the kinetic energy operator ( $\hat{T}$ ) and the potential energy operator ( $\hat{V}$ ) for an electron in the presence of a radially symmetric central potential of an atom  $V(r)$  in spherical coordinates:

$$\begin{aligned}\hat{H}_S &= \hat{T} + \hat{V} = \frac{\hat{p}^2}{2m_e} - eV(r) \\ &= -\frac{\hbar^2}{2m_e} \frac{1}{r} \frac{\partial}{\partial r^2} r + \frac{\hat{L}^2}{2m_e r^2} - eV(r)\end{aligned}\tag{1}$$

In this equation,  $\hbar$  is the reduced Planck's constant,  $m_e$  is the mass of the electron, linear momentum operator is given by  $\hat{p} = -i\hbar\vec{\nabla}$ , where  $\vec{\nabla}$  is the gradient operator for the wavefunction in space. For a central potential in spherical coordinates, the linear momentum can be further decomposed into a radial part and an angular part. The angular momentum operator  $\hat{L}$  is defined as:

$$\hat{L}^2 = -\hbar^2 \left[ \frac{1}{\sin\theta} \frac{\partial}{\partial\theta} \left( \sin\theta \frac{\partial}{\partial\theta} \right) + \frac{1}{\sin^2\theta} \frac{\partial^2}{\partial\phi^2} \right],\tag{2}$$

with the  $\theta$  and  $\phi$  being the polar and azimuthal angles, respectively. The projected angular momentum operator  $\hat{L}_z$  along the z-axis is given by:

$$\hat{L}_z = -i\hbar \frac{\partial}{\partial\phi}.\tag{3}$$



The angular momentum operator  $\hat{L} = \vec{r} \times \hat{p}$  commutes with the Hamiltonian, with the eigenvalues of  $L^2 = l(l+1)\hbar^2$  and  $L_z = m\hbar$  respectively. Here we follow the convention that  $n$  is the principal quantum number,  $l$  is the orbital angular momentum quantum number, and  $m$  is the magnetic quantum number. The eigenfunctions of the Hamiltonian  $\psi_{nlm}(r, \theta, \phi)$  can also be separated into a radial part  $P_{nl}(r)$  and an angular part  $Y_l^m(\theta, \phi)$ :

$$\psi(r, \theta, \phi) = \frac{1}{r} P_{nl}(r) Y_l^m(\theta, \phi), \quad (4)$$

The angular part  $Y_l^m(\theta, \phi)$  are the well-known spherical harmonics that have analytical expressions. In contrast, the radial wavefunction  $P_{nl}(r)$  (except for hydrogen) has to be solved numerically in general with the following ordinary differential equation (ODE):

$$\frac{d^2 P(r)}{dr^2} = \left[ \frac{l(l+1)}{r^2} - \frac{2m_e}{\hbar^2} (E + eV(r)) \right] P(r). \quad (5)$$

The central potential  $V(r)$  includes the Coulomb potential from the nucleus and the potential from the other electrons and is spherically averaged:

$$\begin{aligned} V(r_i) &= \frac{Ne}{r_i} - \sum_{j \neq i}^N \frac{e}{|\vec{r}_i - \vec{r}_j|} \\ &= \frac{Ne}{r_i} - \sum_{j \neq i}^N \int \frac{e |\psi_j(\vec{r}_j)|^2}{|\vec{r}_i - \vec{r}_j|} d\vec{r}_j \\ &= \frac{Ne}{r_i} - \int \frac{e \rho(\vec{r}')}{|\vec{r}_i - \vec{r}'|} d\vec{r}' \end{aligned} \quad (6)$$

where  $N$  is the positive charge of the nucleus and also the number of total electrons for a neutral atom,  $\vec{r}_i$  is the current position of  $i$ th electron that we want to solve the wavefunction for and  $\psi_j(\vec{r}_j)$  is the wavefunction of the  $j$ th electron with the position  $\vec{r}_j$ . To calculate the potential for  $i$ th electron, we need to sum the Coulomb interaction with all other electrons  $j \neq i$ . Furthermore, this

summation is equivalent to the integral of the charge density  $\rho(\vec{r}')$  as a mean field shown in Eq. 6. One may find the equations are nested in a quite interesting manner: solving the wavefunctions of the current  $i$ th electron requires the potential in Eq. 5, which requires solving the wavefunctions and corresponding charge density of all other electrons in Eq. 6. As a consequence, the solution involves an iterative process known as the self-consistent field (SCF) method which is the key step in the Hartree-Fock-Slater approach or modern density functional theory. For bound states ( $E < 0$ ) the radial function is normalized as follows:

$$\int \psi^*(r, \theta, \phi) \psi(r, \theta, \phi) dr = \int_0^\infty P_{nl}^2(r) dr = 1. \quad (7)$$

For continuum states ( $E > 0$ ), the radial function is normalized by matching the asymptotic form as a plane wave at a large distance away from the nucleus:

$$P_{El}(r) \rightarrow \frac{1}{\sqrt{\pi k}} \sin\left(kr - \frac{\pi}{2}l' - \eta \ln(2kr) + \delta_l\right), \quad (8)$$

where  $k = \sqrt{2m_e E}/\hbar$  is the wave vector and  $\eta$  is the Sommerfeld parameter written as:

$$\eta = \frac{Z_\infty e^2}{\hbar v}, \quad (9)$$

with  $Z_\infty = \lim_{r \rightarrow \infty} V(r) r e^{-2}$  which approaches 0 for finite-range potential, and  $v$  is the non-relativistic speed far away from the atom. The phase shift  $\delta_l$  can be calculated by solving the ODE with the boundary condition  $P_{El}(0) = 0$  using the Numerov method and matching the asymptotic form at large  $r$ .

## 2.2. Non-relativistic inelastic electron scattering

Following the derivations given in [19], starting from Fermi's golden rule, the transition rate from initial state  $|i\rangle$  to final state  $|f\rangle$  can be written as:

$$\tau_{i \rightarrow f} = \frac{2\pi}{\hbar} |\langle f | H' | i \rangle|^2 \rho(E_i, E_f), \quad (10)$$

where  $\tau_{i \rightarrow f}$  represents the transition rate (transition probability per unit time).  $\langle f | H' | i \rangle$  denotes the matrix element (in bra-ket notation) of the interaction Hamiltonian  $H'$  between the initial states  $|i\rangle$  and final state  $|f\rangle$  during the transition.  $\rho(E_i, E_f)$  represents the density of states at the initial energy  $E_i$  and the final energy. In this study,  $\rho(E_i, E_f)$  is taken as a delta function  $\rho(E_i, E_f) = \delta(E_i - E_f + \Delta E)$  with  $\Delta E = E_f - E_i$  as the energy difference between initial and final states. Since one can distinguish the probe electron and atomic electron (consequently the exchange effects between them are negligible), the initial or final state can be factorized as the wavefunction of the initial and final orbitals  $\varphi_i$  and  $\varphi_f$  (with  $N$  electrons in their atomic reference system  $r_1 \dots r_N$ ) coupled with the incoming or outgoing plane waves  $\Psi_i$  and  $\Psi_f$  (in the laboratory reference system  $R$ ), with associated wave vector  $\vec{k}_i$  and  $\vec{k}_f$ :

$$\begin{aligned} |i\rangle &= |\varphi_i\rangle |\Psi_i\rangle = |\varphi_i(\vec{r}_1 \dots \vec{r}_N)\rangle \left| e^{i\vec{k}_i \cdot \vec{R}} \right\rangle, \\ |f\rangle &= |\varphi_f\rangle |\Psi_f\rangle = |\varphi_f(\vec{r}_1 \dots \vec{r}_N)\rangle \left| e^{i\vec{k}_f \cdot \vec{R}} \right\rangle. \end{aligned} \quad (11)$$

To satisfy the anti-symmetry requirement (Pauli principle) upon exchange of two electrons in the many-electron system, one typically uses the Slater determinant to represent the atomic electron

wavefunctions  $\varphi_i$  and  $\varphi_f$ . The Slater determinant is written as:

$$|\varphi\rangle = \frac{1}{\sqrt{N!}} \begin{vmatrix} \psi_1(\vec{r}_1) & \psi_2(\vec{r}_1) & \cdots & \psi_N(\vec{r}_1) \\ \psi_1(\vec{r}_2) & \psi_2(\vec{r}_2) & \cdots & \psi_N(\vec{r}_2) \\ \vdots & \vdots & \ddots & \vdots \\ \psi_1(\vec{r}_N) & \psi_2(\vec{r}_N) & \cdots & \psi_N(\vec{r}_N) \end{vmatrix}, \quad (12)$$

The interaction Hamiltonian is taken as the Coulombic potential between the probe electron and the target atom similar to Eq. 6, we can evaluate the transition matrix element by integrating in real space. The real space integral can be simplified using the Fourier transform of the Coulombic potential to the momentum space:

$$\int d^3\vec{R} \frac{e^2}{|\vec{R} - \vec{r}_j|} e^{i\vec{q}\cdot\vec{R}} = \frac{4\pi e^2}{q^2} e^{i\vec{q}\cdot\vec{r}_j}, \quad (13)$$

with  $\vec{R} - \vec{r}_j$  defined as the vector between the probe electron and the  $j$ -th atomic electron. After the integration of the laboratory real space  $\vec{R}$ , the transition matrix element in the momentum space can be evaluated by integration of the atomic reference system for each electron ( $\vec{r}_1 \dots \vec{r}_N$ ) as:

$$\begin{aligned} \langle f|V|i\rangle &= \frac{e^2}{(2\pi)^2 q^2} (\langle \varphi_f | \sum_j^N e^{i\vec{q}\cdot\vec{r}_j} | \varphi_i \rangle - N \langle \varphi_f | \varphi_i \rangle) \\ &= \frac{e^2}{(2\pi)^2 q^2} \langle \psi_f^j | e^{i\vec{q}\cdot\vec{r}_j} | \psi_i^j \rangle. \end{aligned} \quad (14)$$

Several observations can be made: (1) the plane wave with wave vector of the momentum transfer  $\vec{q} = \vec{k}_i - \vec{k}_f$  emerges as a result of the substitution of the explicit form of the initial and final states defined in Eq. 11 into the matrix element in Eq. 10 and Fourier transform of the Coulombic potential in Eq. 13; (2) the contribution to the transition rate from the nuclear electrostatic potential is zero when the initial and final state are orthogonal to each other; (3) only the excited orbital (for

instance, the  $j$ th electron in the equation above) contributes to the transition matrix element due to orthonormality, if we assume all the other orbitals remain unchanged under the frozen core approximation.

The transition rate is dependent on the current density of the quantum system, a more useful definition is the so-called double differential cross-section, which is defined as the probability of the transition per unit solid angle and energy collected. The double differential scattering cross-section (DDSCS) can be written as:

$$\begin{aligned}
\frac{\partial^2 \sigma}{\partial E \partial \Omega} &= \left(\frac{2\pi}{\hbar}\right)^4 (\gamma m_e)^2 \sum_{i,f} \frac{k_f}{k_i} |\langle f | V | i \rangle|^2 \delta(E_i - E_f + \Delta E) \\
&= \frac{4\gamma^2}{a_0^2 q^4} \frac{k_f}{k_i} |S(q, E)|^2, \\
&= \frac{4\gamma^2}{q^2} \frac{R}{\Delta E} \frac{k_f}{k_i} f(q, E)
\end{aligned} \tag{15}$$

where  $\gamma$  is the Lorentz factor for relativistic scalar correction,  $a_0$  is the Bohr radius,  $R$  is the Rydberg energy,  $k_i$  and  $k_f$  are the wave number of the incoming and outgoing plane waves, respectively. To separate the part that is independent of the incoming electron energy, we define the so-called GOS as  $f(q, E)$ :

$$f(q, E) = \frac{\Delta E}{R} \frac{|S(q, E)|^2}{(qa_0)^2}. \tag{16}$$

Here  $|S(q, E)|^2$  is known as the dynamic form factor, which is the squared magnitude of the transition matrix element summed over the final states as:

$$S(q, E) = \sum_{\psi_i, \psi_f} \langle \psi_f | e^{i\vec{q}\cdot\vec{r}} | \psi_i \rangle \tag{17}$$

Note that we take the transition matrix only contributed by the excited orbital and the  $j$  symbol in

Eq. 14 is dropped thereafter for simplicity. The initial and final states of the atomic orbitals are decomposed in terms of radial and angular parts, which has been explained in Sec. 2.1. For the initial states, the summation is applied for the magnetic quantum number  $m$  since we already chose the orbital. For the final states, the summation extends over both the angular quantum number  $l'$  and the magnetic quantum number  $m'$  for each specified final state energy  $E$ .

To derive the dynamic structure factor, one can expand the plane wave using spherical harmonics and integrate the radial and angular parts separately. The plane wave expansion can be written as [64]:

$$e^{iqr} = \sum_{\lambda=0}^{\infty} \sum_{m_{\lambda}=-\lambda}^{\lambda} 4\pi i^{\lambda} (2\lambda + 1) j_{\lambda}(qr) Y_{\lambda}^{m_{\lambda}}(\theta, \phi) \quad (18)$$

where  $j_{\lambda}(qr)$  is the spherical Bessel function of the order  $\lambda$ . First, we can collect all the radial components from the initial states, the final states and the plane wave expansion for the radial integral  $R_{nl,El'}^{\lambda}$ :

$$R_{nl,El'}^{\lambda}(q, E) = \int_0^{\infty} [P_{nl}(r) P_{El'}(r)] j_{\lambda}(qr) dr. \quad (19)$$

Then we can find the angular integral of the products of three spherical harmonics leads to the Wigner 3j symbol ( $\dots$ ), also known as Gaunt coefficients:

$$\int Y_{\lambda}^{m_{\lambda}}(\theta, \phi) Y_{l'}^{m_{l'}}(\theta, \phi) Y_l^{m_l}(\theta, \phi) d\Omega = \sqrt{\frac{(2l+1)(2l'+1)(2\lambda+1)}{4\pi}} \begin{pmatrix} l' & \lambda & l \\ 0 & 0 & 0 \end{pmatrix} \begin{pmatrix} l' & \lambda & l \\ m' & m_{\lambda} & m \end{pmatrix}. \quad (20)$$

When summing the magnetic quantum numbers  $m$  and  $m'$  of the initial and final states in Eq. 20, the expression can be simplified by applying the orthogonal relation of the Wigner 3j symbols,

which results in a delta function and a triangle condition:

$$\sum_{m,m'} \begin{pmatrix} l' & \lambda & l \\ m' & m_\lambda & m \end{pmatrix} \begin{pmatrix} l' & \lambda' & l \\ m' & m'_\lambda & m \end{pmatrix} = \frac{1}{2\lambda+1} \delta_{\lambda'\lambda} \delta_{m_\lambda m'_\lambda} \Delta(l, l', \lambda), \quad (21)$$

with triangle condition  $\Delta(l, l', \lambda) = \begin{cases} 1 & \text{if } |l-l'| \leq \lambda \leq l+l' \\ 0 & \text{otherwise} \end{cases}$

With the radial and angular integral simplified, the dynamic form factor can be written as:

$$|S(q, E)|^2 = \sum_{l'} \sum_{\lambda} [l, l', \lambda] R_{nl, E l'}^\lambda{}^2 \begin{pmatrix} l' & \lambda & l \\ 0 & 0 & 0 \end{pmatrix}^2, \quad (22)$$

where the abbreviated notion of  $[l, l', \lambda] = (2l+1)(2l'+1)(2\lambda+1)$  is used. The dynamic form factor can be physically interpreted as the space-time Fourier transform of the density autocorrelation during the transition, as derived in [19].

The calculations of theoretical spectra, incorporating experimental parameters and Generalized Oscillator Strengths (GOS), will be detailed in Section 4 since the EELS geometric considerations are independent of the choice between Schrödinger or Dirac solutions.

### 3. Theory: relativistic atomic orbitals and inelastic electron scattering

The Dirac equation combines special relativity and quantum mechanics – the cornerstone of modern physics – for relativistic electrons [21]. In this section, we provide an overview of the Dirac equation for atomic orbitals and inelastic scattering. For a comprehensive treatment of this topic, readers are referred to books on relativistic quantum mechanics [65] and recent papers on inelastic electron scattering [50, 66] as here we only outline the essential equations.

### 3.1. Dirac equations for atomic orbitals

The Dirac equation is a first-order differential equation that describes the behavior of relativistic electrons in the presence of an electromagnetic field (minimum coupling), which is written as:

$$(c\gamma^\mu(i\hbar\partial_\mu + eA_\mu) - m_e c^2)\psi = 0, \quad (23)$$

where the summation is implicitly applied over the values of the index  $\mu = 0, 1, 2, 3$  in the Einstein summation notation. For instance, the multiplication of two arbitrary 4-vectors  $\mathbf{A}$  and  $\mathbf{B}$  is written as:

$$\mathbf{A} \cdot \mathbf{B} = A_\mu B^\mu = A^\nu B_\nu = A_\mu \eta^{\mu\nu} B_\nu = a^0 b^0 - \vec{a} \cdot \vec{b}, \quad (24)$$

where  $A_\mu$  are the covariant 4-components and  $A^\mu$  are the contravariant 4-components of the vector  $\mathbf{A}$  in the tensor index notation, which relates to each other via the Minkowski metric  $\eta^{\mu\nu}$ . The multiplication is written in such a manner for the invariance under the Lorentz transformation of the space-time. Back to the Dirac equation,  $\partial_\mu = (\frac{1}{c}\frac{\partial}{\partial t}, \vec{\nabla})$  are the 4-gradient for space-time vectors  $x^\mu = (ct, \vec{r})$ , which gives the 4-momentum  $p_\mu = (\mathbb{E}/c, -\hat{p})$  where  $\mathbb{E}$  is the relativistic energy of the electron.  $A_\mu = (V/c, -\vec{A})$  is the 4-potential consists of electrostatic potential  $V$  and magnetic vector field potential  $\vec{A}$ . The Dirac gamma matrices  $\gamma^\mu$  are defined as:

$$\gamma^0 = \begin{pmatrix} I_2 & 0 \\ 0 & -I_2 \end{pmatrix}, \gamma^j = \begin{pmatrix} 0 & \sigma_j \\ -\sigma_j & 0 \end{pmatrix}, \quad (25)$$

where  $I_2$  is the  $2 \times 2$  identity matrix and  $\sigma_i$  represents the Pauli matrices:

$$\sigma_1 = \begin{pmatrix} 0 & 1 \\ 1 & 0 \end{pmatrix}, \sigma_2 = \begin{pmatrix} 0 & -i \\ i & 0 \end{pmatrix}, \sigma_3 = \begin{pmatrix} 1 & 0 \\ 0 & -1 \end{pmatrix}. \quad (26)$$



We can express the Dirac equation in the 2-component form as follows:

$$\begin{pmatrix} \mathbb{E} + eV(r) - m_e c^2 & -c\boldsymbol{\sigma} \cdot (\hat{\boldsymbol{p}} + e\vec{\boldsymbol{A}}) \\ -c\boldsymbol{\sigma} \cdot (\hat{\boldsymbol{p}} + e\vec{\boldsymbol{A}}) & \mathbb{E} + eV(r) + m_e c^2 \end{pmatrix} \begin{pmatrix} \psi_1 \\ \psi_2 \end{pmatrix} = \begin{pmatrix} 0 \\ 0 \end{pmatrix}, \quad (27)$$

where the upper component  $\psi_1$  and lower component  $\psi_2$  are coupled in Eq. 27. We may define the energy in the excess of the electron rest energy as  $E = \mathbb{E} - m_e c^2$  for ease of comparison with the energy in the Schrödinger equation. For an atomic electron in the presence of a radially symmetric electrostatic potential, we may only consider the electrostatic potential  $V(r)$  and ignore the magnetic vector field potential  $A_\mu$ . In the low-energy limit  $E + eV(r) \ll mc^2$ , we can see that the lower component  $\psi_2$  is much smaller than  $\psi_1$  (as  $\psi_2 \approx \frac{\boldsymbol{\sigma} \cdot \hat{\boldsymbol{p}}}{2m_e c} \psi_1$ ), which is at the order of expectation value of the speed relative to the light  $\frac{\langle v \rangle}{c}$ . For the H atom, this magnitude is at the fine-structure constant ( $\sim 1/137$ ) but gradually increases with atomic number as the momentum increases. Hence, the upper and lower components are often referred to as the large and small components, respectively.

The solution can be factorized into radial part and angular parts:

$$\boldsymbol{\psi} = \frac{1}{r} \begin{pmatrix} P_{n\kappa}(r) \mathcal{Y}_{jlm}(\boldsymbol{\theta}, \boldsymbol{\phi}) \\ iQ_{n\kappa}(r) \mathcal{Y}_{j'l'm}(\boldsymbol{\theta}, \boldsymbol{\phi}) \end{pmatrix}, \quad (28)$$

As  $l$  is no longer a good quantum number in the Dirac equation. Here, we introduce the total angular momentum operator defined as  $\hat{\boldsymbol{J}} = \hat{\boldsymbol{L}} + \hat{\boldsymbol{S}}$  with its eigenvalue  $J^2 = (j+1)j\hbar^2$  and  $J_z = m_j\hbar$ , and  $j$  is bounded by  $|l-s| \leq j \leq |l+s|$  in magnitude.  $\hat{\boldsymbol{S}}$  is the spin operator with eigenvalues of  $S^2 = s(s+1)\hbar^2$  and  $S_z = m_s\hbar$ , where  $s = 1/2$  and  $m_s = -1/2$  or  $1/2$  for electron.  $P_{n\kappa}(r)$  and  $Q_{n\kappa}(r)$  are the radial parts of the large and small components, respectively. The relativistic

quantum number  $\kappa$  is defined as:

$$\kappa = (l - j)(2j + 1) = \begin{cases} -l - 1, & \text{if } j = l + \frac{1}{2} \text{ (spin up)} \\ l, & \text{if } j = l - \frac{1}{2} \text{ (spin down)} \end{cases}. \quad (29)$$

For the angular part,  $\mathcal{Y}_{jlm}(\theta, \phi)$  represents the spinor spherical harmonics (note in the small component  $l' = 2j - l$  in Eq. 28), which can be written as:

$$\mathcal{Y}_{jlm}(\theta, \phi) = \sum_{m_l, m_s} \langle l, 1/2, m_l, m_s | j, m_j \rangle Y_l^{m_l}(\theta, \phi) \chi_{\frac{1}{2}, m_s}, \quad (30)$$

where  $\langle l, 1/2, m_l, m_s | j, m_j \rangle$  is the Clebsch-Gordan coefficient,  $Y_l^{m_l}(\theta, \phi)$  is the usual spherical harmonics with  $m_l = m_j - m_s$  and  $\chi_{\frac{1}{2}, m_s}$  is the spin eigenfunction of a spin 1/2 particle:

$$\chi_{\frac{1}{2}, +\frac{1}{2}} = \begin{pmatrix} 1 \\ 0 \end{pmatrix} \quad \text{and} \quad \chi_{\frac{1}{2}, -\frac{1}{2}} = \begin{pmatrix} 0 \\ 1 \end{pmatrix} \quad (31)$$

For the radial part, the Dirac equation can be written as coupled ODE equations:

$$\begin{aligned} \frac{dP_{n\kappa}}{dr} &= -\frac{\kappa}{r} P_{n\kappa} + \frac{E + 2m_e c^2 + eV}{c\hbar} Q_{n\kappa}, \\ \frac{dQ_{n\kappa}}{dr} &= \frac{-E - eV}{c\hbar} P_{n\kappa} + \frac{\kappa}{r} Q_{n\kappa}. \end{aligned} \quad (32)$$

For the bound state ( $E < 0$ ), the radial part can be normalized as:

$$\int_0^\infty (P_{n\kappa}^2(r) + Q_{n\kappa}^2(r)) dr = 1. \quad (33)$$

For the free state ( $E > 0$ ), the radial part can be normalized by matching the asymptotic behavior:

$$P_{E\kappa'} \rightarrow \frac{1}{\sqrt{\pi k}} \sin\left(kr - \frac{\pi}{2} \kappa' - \eta \ln(2kr) + \delta_{\kappa'}\right), \quad (34)$$

where  $k = \sqrt{E(E + 2m_e c^2)}/\hbar c$  is the relativistic wave number, and  $\delta_{\kappa'}$  is the phase shift.  $\eta$  is the relativistic Sommerfeld parameter with the corresponding relativistic speed in Eq. 9. In the

low-energy limit,  $E + eV \ll m_e c^2$ , the radial part can be written as [66]:

$$Q_{n\kappa} = \frac{c\hbar}{2 m_e c^2} \left( \frac{\kappa}{r} P + \frac{dP}{dr} \right) \quad (35)$$

and

$$\frac{d^2 P_{n\kappa}(r)}{dr^2} = \left[ \frac{\kappa(\kappa+1)}{r^2} - \frac{2m_e}{\hbar^2} (E + eV(r)) \right] P_{n\kappa}(r) \quad (36)$$

Note that  $\kappa(\kappa+1) = l(l+1)$ , reducing the upper component  $P_{n\kappa}(r)$  radial equation to the Schrödinger radial equation as in Eq. 5.

### 3.2. Relativistic inelastic electron scattering

From the perspective of electrodynamics, the motion of a charged particle induces electric and magnetic fields and hence perturbs the interaction Hamiltonian. Instead of taking the rigorous quantum field theory, here we follow perturbation theory due to its simplicity, as well outlined in [31, 54, 55, 56]. The DDSCS for inelastic electron scattering is given by:

$$\frac{\partial^2 \sigma}{\partial E \partial \Omega} = \left( \frac{2\gamma}{a_0} \right)^2 \frac{1}{(q^2 - (\Delta E/\hbar c)^2)^2} \frac{k_f}{k_i} \sum_{\psi_i, \psi_f} |\langle \psi_f | e^{i\vec{q}\vec{r}} \left( 1 - \frac{\hat{p}\vec{v}_0}{m_e c^2} \right) | \psi_i \rangle|^2 \delta(E_i - E_f + \Delta E), \quad (37)$$

where  $v_0$  is the velocity of the incident probe electron with energy  $E_0$ . By comparing Eq.37 with the non-relativistic case in Eq. 15, we can note that  $q^2$  is replaced by  $q^2 - (\Delta E/\hbar c)^2$  and there is an extra term  $\frac{\hat{p}\vec{v}_0}{m_e c^2}$ , which originates from the perturbation of the fast moving charge under the Coulomb gauge leading to the contraction of the scattering vector in the direction of the incident beam (retardation effect) [55]. This is equivalent to the z-component of the 4-transition current under the Lorentz gauge [56]. The relativistic effect of incident fast electron plays a critical role in the experimental observation of the magic angle in EELS [55] and the detailed intensity

distribution in energy-filtered electron diffraction [56], thus it is important to include it correctly for quantitative work. By projecting the contribution of  $\frac{\hat{p}\vec{v}_0}{m_e c^2}$  to directions that are parallel and normal to the incident electron, we can further simplify the DDSCS as proposed in [31, 54]:

$$\frac{\partial \sigma}{\partial E \partial \Omega} = \left(\frac{2\gamma}{a_0}\right)^2 \frac{k_f}{k_i} \left[ \frac{1}{q^4} + \frac{\beta_t^2 (\Delta E / \hbar c)^2}{(q^2 - (\Delta E / \hbar c)^2)^2} \right] \sum_{\psi_i, \psi_f} |\langle \psi_f | e^{i\vec{q}\vec{r}} | \psi_i \rangle|^2, \quad (38)$$

where  $\beta_t$  is the transverse component of the incident electron velocity (in units of the speed of light)  $\beta = v_0/c$  with respect to the scattering vector  $\vec{q}$ :

$$\beta_t^2 = \beta^2 - \frac{\Delta E^2}{(cq)^2} \left( 1 + \frac{(cq)^2 - \Delta E^2}{2\Delta E(E_0 + m_e c^2)} \right) \quad (39)$$

For the orbital relativistic effects, the transition matrix element must account for the Dirac solution, which includes both the large and small components [31]. As a consequence, the radial overlap integral is changed from Eq. 19 to:

$$R_{n\kappa, E\kappa'}^\lambda(q, E) = \int_0^\infty [P_{n\kappa}(r)P_{E\kappa'}(r) + Q_{n\kappa}(r)Q_{E\kappa'}(r)] j_\lambda(qr) dr. \quad (40)$$

For the angular part, the spherical harmonics in the Schrödinger solution are now replaced by the spinor spherical harmonics in the Dirac solution. This addition introduces a Wigner 6j  $\left\{ \dots \right\}$  term when integrating over the angle and summing over the states. Overall, the dynamic form factor in the Dirac solution is given by:

$$|S(q, E)|^2 = \sum_{l'} \sum_{\lambda} \sum_{\kappa'} [l, l', j', \lambda] R_{n\kappa, E\kappa'}^\lambda{}^2 \begin{pmatrix} l' & \lambda & l \\ 0 & 0 & 0 \end{pmatrix}^2 \left\{ \begin{matrix} j & \lambda & j' \\ l' & \frac{1}{2} & l \end{matrix} \right\}^2, \quad (41)$$

The GOS still follows the same definition as in the non-relativistic case in Eq. 16.

To check we have the correct implementation of the relativistic correction defined in Eq. 38, we can use the analytical expression for the relativistic correction ratio under dipole approxima-

tion, which is defined as the ratio of the scattering cross-sections with and without the relativistic electrodynamics effects. This ratio is given by [50, 55, 56]:

$$\sigma_{\text{ratio}}(\Delta E) = \frac{\sigma_{\text{rel}}(\Delta E)}{\sigma_{\text{conv}}(\Delta E)} = \left[ \ln \left( 1 + \frac{x_{\theta}}{1 - \beta^2} \right) - \frac{\beta^2 x_{\theta}}{1 - \beta^2 + x_{\theta}} \right] \frac{1}{\ln(1 + x_{\theta})}, \quad (42)$$

where  $x_{\theta} = \theta_0^2/\theta_E^2$  is the squared ratio of the collection angle  $\theta_0$  to the characteristic angle  $\theta_E$ , which is written as:

$$\theta_E = \frac{\Delta E}{\gamma m v_0^2} \quad (43)$$

In Section 6.2, we will examine the relativistic correction ratio for cross-sections under different experimental conditions.

#### 4. EELS geometry parameters in momentum space integration

In this section, we will explain how to consider the experimental EELS geometry (i.e. EELS collection angle and STEM convergence angle) for cross-section calculations. From the dynamic form factor in Eq. 22 and Eq. 41 (or the associated GOS in Eq. 16), one can integrate over the EELS collection angle to obtain the differential cross section as a function of energy loss [19]. The differential cross section is given by:

$$\frac{d\sigma}{dE} = \frac{4\pi\gamma^2}{k_i^2} \int_{Q_{\min}}^{Q_{\max}} \frac{|S(q, E)|^2}{Q} d(\ln(Q)), \quad (44)$$

where we take  $Q = (a_0 q)^2$  for ease of integration. From the scattering geometry, we can set the upper and lower limits of the integration as:

$$\begin{aligned} q_{\min} &= k_i - k_f, \\ q_{\max} &= \sqrt{k_i^2 + k_f^2 - 2k_i k_f \cos(\beta_0)}, \end{aligned} \quad (45)$$

as the minimum scattering angle is zero and the maximum scattering angle is bound by the EELS collection aperture  $\beta_0$ . The differential cross section as a function of energy loss is used to fit and quantify the experimental EELS spectra.

For plane wave illumination in TEM, The above Eq. 44 is sufficient. For STEM convergent beam illumination, we need to take into account the finite angle of both the convergence angle and collection angle, which can be performed by the geometric correction procedure proposed by Kohl [67]. In this approach, we consider the STEM illumination as a collection of plane waves with their corresponding wave vectors bounded by the convergence angle  $\alpha_0$ . The EELS collection angle  $\beta_0$  defines the maximum angle relative to the incident direction to be recorded by the detector. For a given scattering angle  $\theta$ , there could be different combinations of incident angle and exit angles allowed by the geometry. As a consequence, the DDSCS should be multiplied by a correction factor corresponding to those combinations. Based on the geometric interpretation, this problem is equivalent to the intersection area of two circles – one with a radius of  $\alpha_0$  and another with a radius of  $\beta_0$  and they are separated by a distance of  $\theta$ . The resulting correction factor is a cross-correlation function, which is written as [67]:

$$F_{\text{BF}}(\alpha_0, \beta_0, \theta) = \begin{cases} \theta^2 / \alpha_0^2, & \text{for } 0 \leq \theta \leq |\alpha_0 - \beta_0|, \\ \pi^{-1} [\arccos(x) + (\beta_0^2 / \alpha_0^2) \arccos(y) \\ - (1/2\alpha_0^2) \sqrt{4\alpha_0^2\beta_0^2 - (\alpha_0^2 + \beta_0^2 - \theta^2)^2}], & \text{for } |\alpha_0 - \beta_0| < \theta < \alpha_0 + \beta_0, \\ 0, & \text{otherwise.} \end{cases} \quad (46)$$

where

$$\begin{aligned}
\theta_{<} &= \min(\alpha_0, \beta_0), \\
x &= \frac{\alpha_0^2 + \theta^2 - \beta_0^2}{2\alpha_0\theta}, \\
y &= \frac{\beta_0^2 + \theta^2 - \alpha_0^2}{2\beta_0\theta}.
\end{aligned} \tag{47}$$

The EELS correction factor  $F_{BF}$  (closely related to the contrast transfer function of bright field incoherent imaging) is used to correct the DDSCS for a given set of scattering angles in the STEM-EELS geometry. The effective partial scattering cross-section after integration in the momentum space is written as [67]:

$$\frac{d\sigma_{\text{eff}}}{dE} = \int_0^{\alpha_0 + \beta_0} F_{BF}(\alpha_0, \beta_0, \theta) \frac{d^2\sigma}{dE d\Omega} 2\pi\theta d\theta, \tag{48}$$

or in terms of the Q space integral as in Eq. 44

$$\begin{aligned}
\frac{d\sigma_{\text{eff}}}{dE} &= \frac{4\pi\gamma^2}{k_i^2} \int_{Q_{\min}}^{Q_{\max}} \frac{|S(q, E)|^2}{Q} F_{BF}(\alpha_0, \beta_0, \theta) d(\ln(Q)), \\
\text{with } \theta &= \arccos\left(\frac{k_i^2 + k_f^2 - q^2}{2k_i k_f}\right),
\end{aligned} \tag{49}$$

$$q_{\min} = k_i - k_f,$$

$$q_{\max} = \sqrt{k_i^2 + k_f^2 - 2k_i k_f \cos(\alpha_0 + \beta_0)},$$

## 5. Computational details

In this study, we only perform GOS calculations for single atoms, thereby disregarding the solid state effects in EELS. The atomic orbital calculations are performed using the Flexible Atomic Code (FAC) [68] package. To solve the Dirac radial wavefunction as described in Eq. 32, FAC considers the local atomic potential as a combination of the electron-nucleus and electron-electron Coulomb interactions. The solution is computed through a self-consistent Dirac–Fock–Slater

method within a modified local density approximation for the correct asymptotic behavior of the exchange energy [68]. We take the bound state of the target orbital as the initial state and the continuum state as the excited state. Continuum states are treated in the distorted-wave approximation [68]. Fermi's golden rule employed a delta function to represent the density of states, thus ignoring the fine structures. In addition, the orthogonality of the initial and final states is necessary to exclude the contribution of the nucleus in Eq. 14, which otherwise causes a divergence of the cross-sections when momentum transfer approaches zero. To ensure orthogonality, we take the frozen core approximation that assumes the potential remains unchanged for the initial and final states, which means only the excited orbital contributes to the transition matrix in Eq. 14. The calculated large and small components are used in the Eq. 40 to compute the transition matrix element. The convergence is checked by including final states (summation of  $\kappa'$  in Eq. 41) until the contribution of the last final state falls below 0.1%.

The GOS calculation is computationally intensive since we need to sum over different final states for each energy loss. To accelerate the process, we developed a highly efficient parallelization scheme to take advantage of modern computer with multiple CPUs. Specifically, the calculation of the transition matrix is evaluated using the multi-processing of different energy losses. For a given energy loss, multi-threading is used for all the final states  $\kappa'$  until convergence. We implemented a dynamic predicting, caching, and dumping strategy for the number of final state wavefunctions needed to manage memory usage during parallelization. After optimization, the computation of the entire database takes about 2 days on a desktop (intel i9-7900X 10 CPUs @4.5GHz), and less than 4 hours on a single node on a high-performance computing cluster (2x 64-core AMD Epyc 7H12 CPU @2.6 GHz).



We constructed the GOS database for all elements with atomic number  $Z$  ranging from 1 to 118 and all available shells. This resulted in a total of 2143 entries tabulated as a function of energy loss  $\Delta E$  and momentum transfer  $q$  with fine sampling. More specifically, we computed the GOS in an energy range of 0.01 - 4000 eV above the ionization energy with 128 sampling points and an adaptive momentum range of  $(q_{\min}, q_{\max})$  with 256 sampling points. Both energy and momentum sampling follows a log sampling scheme, as also done in [26, 28, 60]. The minimum momentum transfer  $q_{\min}$  is in the direction of the incident beam, defined as:

$$q_{\min} = \frac{\Delta E_{\min}}{\hbar c}, \quad (50)$$

where  $\Delta E_{\min}$  corresponds to the minimum energy loss which is the ionization energy. The maximum momentum sampling  $q_{\max} = 2q_r$ , where  $q_r$  is the momentum transfer at the Bethe ridge for a given energy loss [10]:

$$(a_0 q_r)^2 = \frac{\Delta E}{R} + \frac{\Delta E^2}{2m_e c^2 R}. \quad (51)$$

Adaptive momentum sampling is developed in such a manner to maximize the physical information for a given finite number of sampling points. For instance, an ionization event is always associated with a scattering vector larger than  $q_{\min}$ , thus sampling below the lower limit would be pointless. Also, the transition probability beyond  $q_{\max}$  is well decayed to negligible. Note that the  $(q_{\min}, q_{\max})$  is elemental edge dependent, so the sampling has to be adaptive instead of fixed for all the edges. The database was saved in an HDF5 file following the GOSH file format [62] so that users can switch easily between different variations of GOS databases.

We also used the GPAW software to calculate the all-electron Schrödinger DFT using the projector augmented wave method [69] with generalized gradient approximation of the potential

[70]. The DFT calculations are performed to compare the orbital energies with Dirac results in this work but not for GOS computation.

## 6. Results and discussions

In this section, we will first give an overview of the Dirac-based GOS database compared to other Schrödinger solutions in Sec. 6.1, highlighting the effects of SOC on the ionization energy, the wavefunctions, and the GOS. In Sec. 6.2, we will demonstrate the necessity of considering the relativistic effects of fast electrons in quantitative EELS. In Sec. 6.3, we will compare the computed scattering cross-sections from the Dirac-based GOS with other Schrödinger-based GOS databases, showing the general agreement and fine differences. In Sec. 6.4, we will provide a step-by-step guide on how to use the Dirac-based GOS database for EELS quantification.

### 6.1. Overview of the Dirac-based GOS database

A distinct improvement of our GOS database is the large energy-momentum range with a fine sampling. Such sampling requires significant computational efforts, which once limited the HF GOS, are now more manageable owing to the rapid development of computation hardware and highly optimized parallelization algorithms. For comparison, Fig. 1 shows the GOS database for the C-K edge constructed previously based on (a) the HF solution (used in Gatan Digital Micrograph), (b) the DFT solution, and (c) the Dirac solution. For this particular case, HF GOS reaches a maximum energy of 200 eV above the onset with 12 sampling points and a maximum momentum of  $12.7 \text{ \AA}^{-1}$  with 20 sampling points. For conventional cross-section integration, one may argue that 200 eV should be sufficient for an integration energy window but not enough

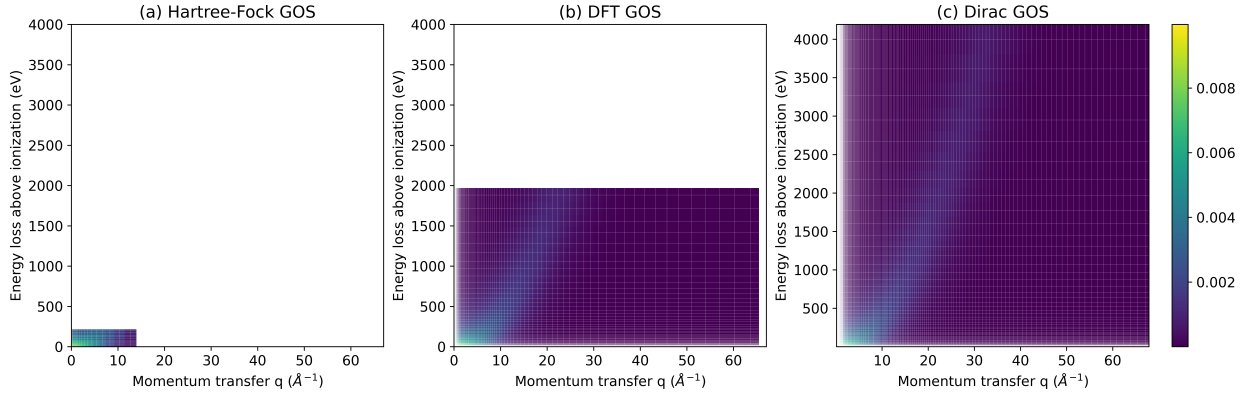


Figure 1: Comparison of the GOS databases for the C K-edge calculated from (a) the Hartree-Fock solution, (b) the DFT solution, and (c) our Dirac solution as a function of momentum transfer and energy loss above the ionization. The sampling grid is indicated by the white lines. The log sampling is dense at low energy loss and low momentum transfer region, where most experiments focus on.

for model-based fitting. In contrast, the Dirac GOS extends the sampling to 4000 eV above the ionization and  $67 \text{ \AA}^{-1}$  with 128 and 256 sampling points, respectively. The sampling scheme enables the clear visualization of the Bethe ridge with locally high transition probabilities in a parabolic region ( $\Delta E \sim q^2$ ) in the energy-momentum space. In practice, the extended energy loss range of GOS can be useful for the simultaneous model-based fitting of multiple elements. For example, the presence of carbon support is common in TEM sample preparation. In the case of a limited GOS energy range, the background fitting may only use the pre-edge region to extrapolate a power law function instead of taking the exact decaying tail of the C K-edge, which introduces additional bias for model-based fitting of multiple elements. Fine sampling is also helpful for the accurate generation of the EELS cross-sections and consequently spectrum quantification. Note that the large sampling range and fine sampling step is a common practice in modern computing, which is also available at recent DFT-based GOS [60] shown in Fig. 1 (b) but with a momentum

sampling fixed around  $63 \text{ \AA}^{-1}$  and a smaller energy range (up to  $\sim 1900 \text{ eV}$ ) for all elements.

Table 1: The onset energies of different edges, with the experimental measurement from EELS Atlas, XPS, and the theoretical predictions from Dirac and all-electron Schrödinger solutions.

Element	Orbital	Edge	Experimental Measurement (eV)		Theoretical Calculation (eV)	
			EELS Atlas[71]	XPS[72]	Dirac	Schrödinger
Ti	$2p_{1/2}$	$L_2$	462	460	454	444
	$2p_{3/2}$	$L_3$	456	454	448	
Ag	$3d_{3/2}$	$M_4$	373	374	370	358
	$3d_{5/2}$	$M_5$	367	368	364	
Au	$4f_{5/2}$	$N_6$	86	88	84	81
	$4f_{7/2}$	$N_7$	83	84	80	

The key benefit of employing the Dirac equation lies in its intrinsic inclusion of relativistic effects, rather than applying corrections to the Schrödinger equation. In the context of EELS, a notable advantage is the precise prediction of spin-orbit splittings of different elements. Table 1 presents Ti  $L_2/L_3$ , Ag  $M_4/M_5$ , and Au  $N_6/N_7$  edges with experimental measurements from the EELS Atlas [71], X-ray Photoelectron Spectroscopy (XPS) [72] and theoretical ionization energies calculated using the Dirac and Schrödinger equations for each orbital. For instance, the Ti  $L_2$  edge is observed to be 6 eV higher than the  $L_3$  edge in both EELS and XPS, with the splitting known due to spin-orbit coupling (SOC) [63]. From the perspective of applying relativistic corrections to the Schrödinger equation, a spin-down electron has lower energy than that of a spin-up electron with a

SOC contribution that scales with  $\sim \langle \hat{L} \cdot \hat{S} \rangle$ . Such measurements align well with predictions from the Dirac equation (454 / 448 eV). In contrast, the Schrödinger equation predicts a single onset energy for the 2p orbital regardless of spin variations. However, it's important to note that the Dirac values don't exactly match experimental measurements. This discrepancy arises because we only performed the calculation for a single neutral atom, thereby ignoring chemical shifts (as observed in ions with different oxidation states, for example, the Ti edges were measured from TiO<sub>2</sub> in the EELS Atlas) and solid state effects (resulting from many-body perturbations by surrounding atomic potentials). Nevertheless, the Dirac equation accurately predicts the energy difference from splitting as observed experimentally. This trend is similarly observed in the M<sub>4</sub>/M<sub>5</sub> edge of Ag and N<sub>6</sub>/N<sub>7</sub> edge of Au. Note that we did not yet consider the effect of Zeeman splitting of the strong magnetic field in the objective lens of a modern microscope, which could be interesting for further study. To further verify the match between theory and experimental measurements systematically, Fig. 2(a) plots the Dirac predicted ionization energy against the edge onset energy all available in EELS Atlas, containing 1105 pairs of data in total and covering a wide range of atomic numbers (1-96) and energies (11-34561 eV). As discrepancies between atomic calculations and experimental measurement are expected due to the aforementioned chemical shifts and solid-state effects, small deviations from the exact match (as indicated by the dashed line) are observed in Fig. 2(b). A histogram of the relative residual between the Dirac predictions and EELS Atlas values is plotted inside of Fig. 2(b), showing the deviations (mean: 0.2%, standard deviation: 7%) are well bounded. Further investigation shows that those cases with large deviations are mainly from the O edges of heavy elements (i.e. transition elements in the La and Ac families), which are also visible in Fig. 2(a). The general trend of residual can be captured fairly well with

linear regression as indicated by the red solid line. We can also make a reasonable estimation for other edges not recorded in the EELS Atlas by applying the same slope ( $\sim 1.01$ ) from the linear regression to the Dirac ionization energy.

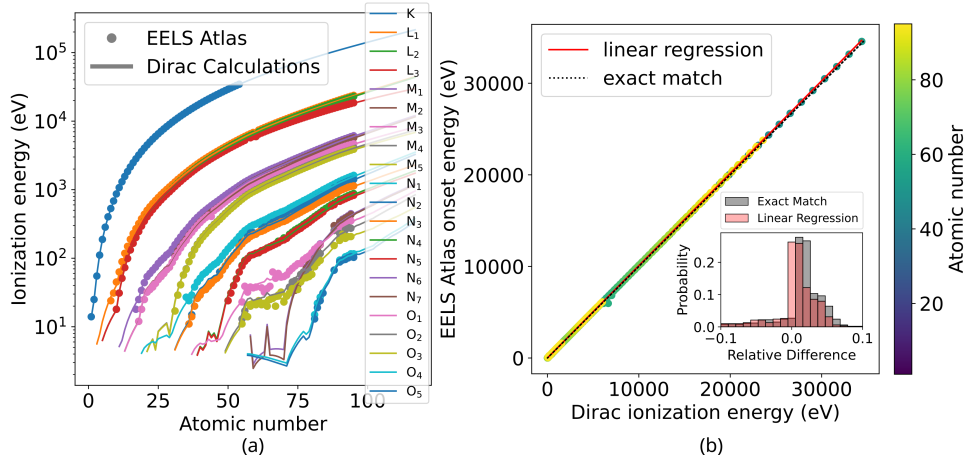


Figure 2: (a) Comparison of the Dirac predicted ionization energy with the EELS Atlas for all available elements ( $Z=1-96$ ). (b) A plot of the predicted ionization energies against the edge onset energies from EELS Atlas to demonstrate the linear correlation. The variation of atomic number can be visualized by the color bar. The black dashed line indicates the exact match between theory and experiment. The red solid line represents the linear regression of the data. The probability histogram of the relative residual between the Dirac calculation and EELS Atlas is plotted inside for the exact match and after linear regression.

In addition to the precise onset energy, the Dirac solution is expected to capture the accurate charge distribution due to relativity. The Dirac solution has large and small components, where the large component is much more significant and can be approximated to the Schrödinger solution at the low-speed limit as shown in Eq. 5 and Eq. 36. However, this does not mean the small component is not important, especially when the core-shell electron of heavy elements approaches

the speed of light. The expectation value of the speed of an orbital electron  $\langle v \rangle$  is defined as:

$$\langle v \rangle = \frac{\langle p \rangle c^2}{\sqrt{m_e^2 c^4 + \langle p^2 \rangle c^2}}. \quad (52)$$

Fig. 3(a) shows that orbital electrons (up to 5g orbital)  $\langle v \rangle$  increase with the atomic number, reaching a considerable fraction of the speed of light for heavy elements. For instance, the 1s electron of Au can reach  $\sim 57\%$  of the speed of light. Ranking the speed among different orbitals, one may observe that the 1s<sub>1/2</sub> electron is always associated with the highest speed as it directly faces the nucleus (with the lowest expectation value of the distance from nucleus  $\langle r \rangle$  and therefore least screening effects caused by other electrons). This is then followed by the 2s<sub>1/2</sub> and 2p<sub>1/2</sub> spin-down electrons with similar velocities. The 2p<sub>1/2</sub> electron has a noticeably lower speed compared to that of 2p<sub>3/2</sub>. There are additional orbital pairs with similar speeds for 3s<sub>1/2</sub>-3p<sub>1/2</sub>, 3p<sub>3/2</sub>-3d<sub>3/2</sub>, etc. This is not surprising as such pairs have the same total angular momentum  $j$  and relativistic quantum number term  $(\kappa + 1)\kappa$ . Consequently, they have the same effective potential and kinetic energy following Eq. 36 in the low energy limit. For the Dirac solution, the fast core-shell electrons are accompanied by the increasing contribution of the small component shown in 3(b). Here we define the contribution of the small component  $\zeta$  for a given orbital  $n\kappa$  as:

$$\zeta = \frac{\int_0^\infty (Q_{n\kappa}^2(r)) dr}{\int_0^\infty (P_{n\kappa}^2(r) + Q_{n\kappa}^2(r)) dr} = \int_0^\infty (Q_{n\kappa}^2(r)) dr, \quad (53)$$

since the wavefunctions are already normalized in Eq. 33. Fig. 3(c-e) shows the radial charge density for three typical elements ranging from light to heavy (Si, Ag, and Au). As expected, the large component always dominates the charge distribution. In contrast, the small component is negligible for Si, but becomes noticeable for Ag and significant for Au, mainly for core-shell electrons close to the nucleus as indicated by the orbital decomposition shaded in different colors.

The direct consequence of the Dirac solution for GOS is reflected in the radial integral of Eq. 40, where the small component contributes to the transition matrix element. Further analysis of the  $L_2/L_3$  edges shows that the contribution of small components to the GOS is negligible for Si, approximately 1% for Ag, and 3-5% for Au (depending on the spin), which is proportional to the contribution of the small components to the charge distribution (Si: 0.03%, Ag 0.6%, Au 2%).

The spin variation also yields different wavefunctions and hence different transition matrixes and GOS, in contrast to a single matrix from the Schrödinger solution. In Fig. 4(a), the electron ionization energy is plotted as a function of the orbital and spin variations, wherein Fig. 4(b-d) plots the radial wavefunctions for the bound and continuum states. The significance of energy splitting and deviation from the Schrödinger solution is a direct indication of the strength of SOC, which is particularly pronounced for p orbitals and less obvious for higher orbitals (like d orbitals) in general due to electron screening (note energies plotted on a log scale). For radial wave functions of bound states, the  $2p_{1/2}$  orbital is contracted inward compared to the  $2p_{3/2}$  orbital for both the large and small components as shown in Fig. 4(b). In contrast, the large components for 3d orbitals are similar regardless of the spin, while its small component is slightly contracted inward for  $3d_{3/2}$  electron compared to  $3d_{5/2}$  as shown in Fig. 4(c). To calculate the matrix elements, the bound state wavefunctions will be integrated with different final continuum states for each energy, one of which is shown in Fig. 4(d) for a final state angular quantum number  $l' = 2$  with spin-up/down at 10 eV above the ionization energy. The highly oscillating nature of the continuum state (with frequency increases with increasing energy loss) and spherical Bessel function (with frequency increases with increasing momentum transfer) suggests that a slight shift in the radial wavefunction of the highly localized bound state can result in a remarkable change in the integral



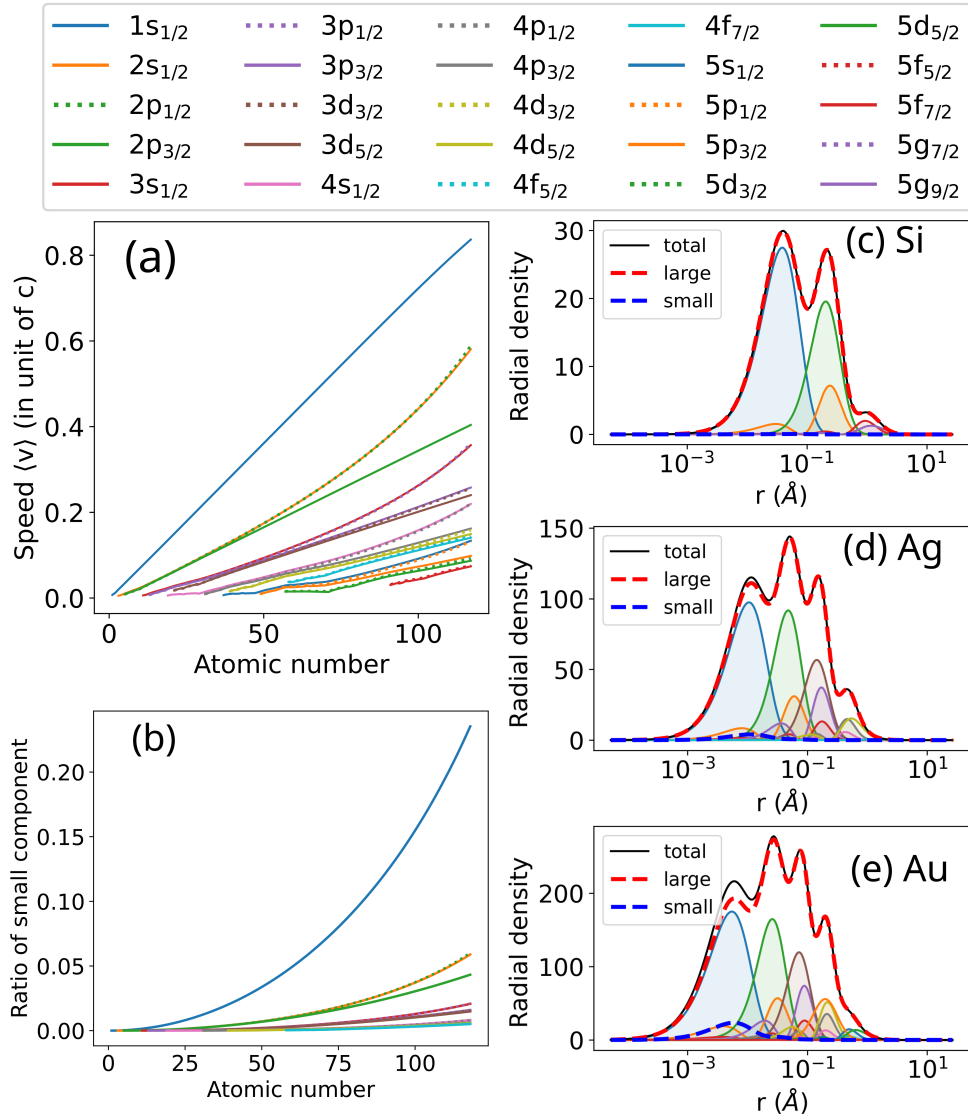


Figure 3: (a) The expectation value of relativistic speed  $\langle v \rangle$  of the orbital electrons (up to 5g) for elements ( $Z=1-118$ ) in the periodic table. The spin-down electron is indicated by the dotted line. (b) Contribution of the small component to the charge density for each orbital of all elements. (c-e) The radial charge density for three typical elements from light to heavy (Si, Ag, and Au). The large component is shown in blue and the small component is shown in red. The orbital decomposition is indicated by the shaded area in different colors.

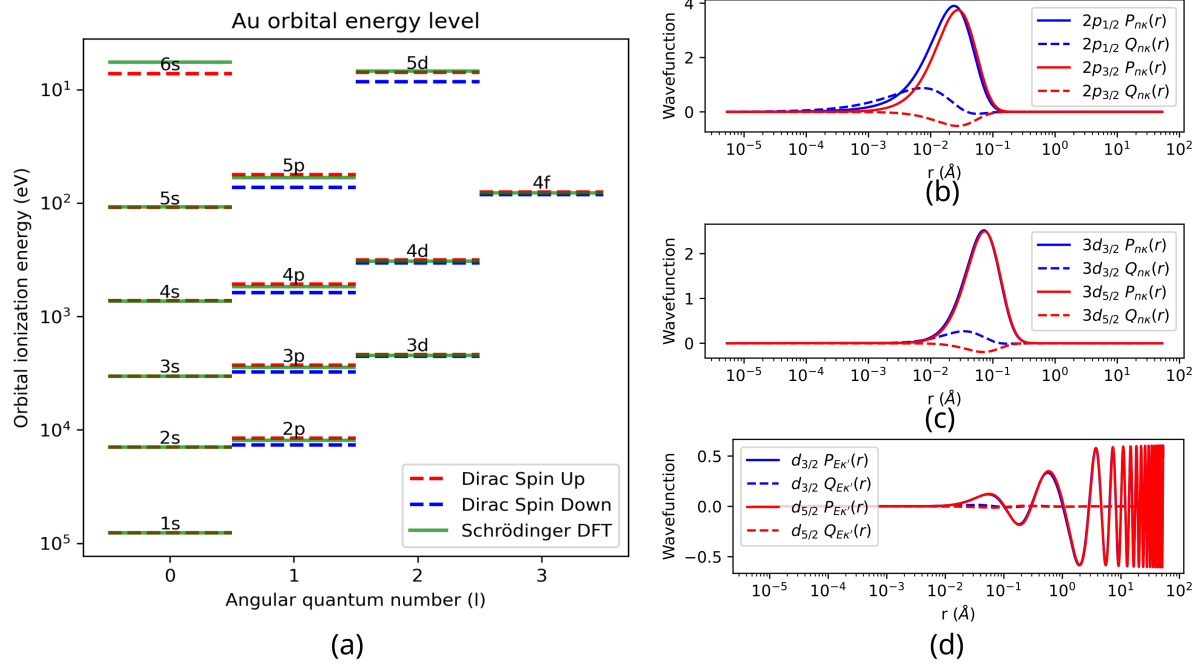


Figure 4: (a) Orbital energy level for Au as a function of angular quantum number with spin variations. The red/blue shaded line indicates spin up/down Dirac solution, while the green solid line indicates the Schrödinger all-electron DFT solution. The radial wavefunctions for (b) the 2p orbital, (c) the 3d orbital, and (d) continuum state d orbital at 10 eV with spin variations.

wavefunction overlaps for bound states with different spin quantum numbers.

To investigate how spin variation affects the GOS, Fig. 5 demonstrates the contributions of final states with different angular quantum numbers and spin variations, plotted as a function of energy loss and momentum transfer. Fig. 5(a-b) shows the decomposition of the contributions from final states for the Au  $L_2/L_3$  case at 10 eV and 4000 eV above the edge onset. At low energy loss, the dipole transition  $\Delta l' = |l - l'| = 1$  dominates the GOS as expected. However, for high energy loss, there are notable contributions from final states with other  $l'$  leading to the emergence of a peak at high momentum transfer known as the Bethe ridge [10]. In the case of Au, the difference of spin reaches 20% for  $L_2/L_3$  edges, but it can be higher for a heavier element (like actinium can be over 40%). This difference in GOS is not surprising, as the spin-down electron is closer to the nucleus with a higher ionization energy due to SOC, its excitation is expected to have a lower transition probability compared to the spin-up electron. In contrast, the ratio of spin-down/up is close to 0.95 for  $M_4/M_5$  edges which is a result of negligible spin variations in their wavefunctions shown in Fig. 4(c).

## 6.2. Relativistic electrodynamics for EELS cross-section calculations

The relativistic effects in electrodynamics significantly enhance the scattering cross-section, particularly noticeable at low angles and high energies. Fig. 6(a) shows the relativistic and non-relativistic double differential cross sections for silicon K-edge at different acceleration voltages, showing a small angle peak, which becomes more pronounced with increasing acceleration voltage, negligible at 100 keV but not for higher voltages. As explained in previous studies [54, 55, 56], this relativistic correction is obtained when applying Lorentz gauge for a moving

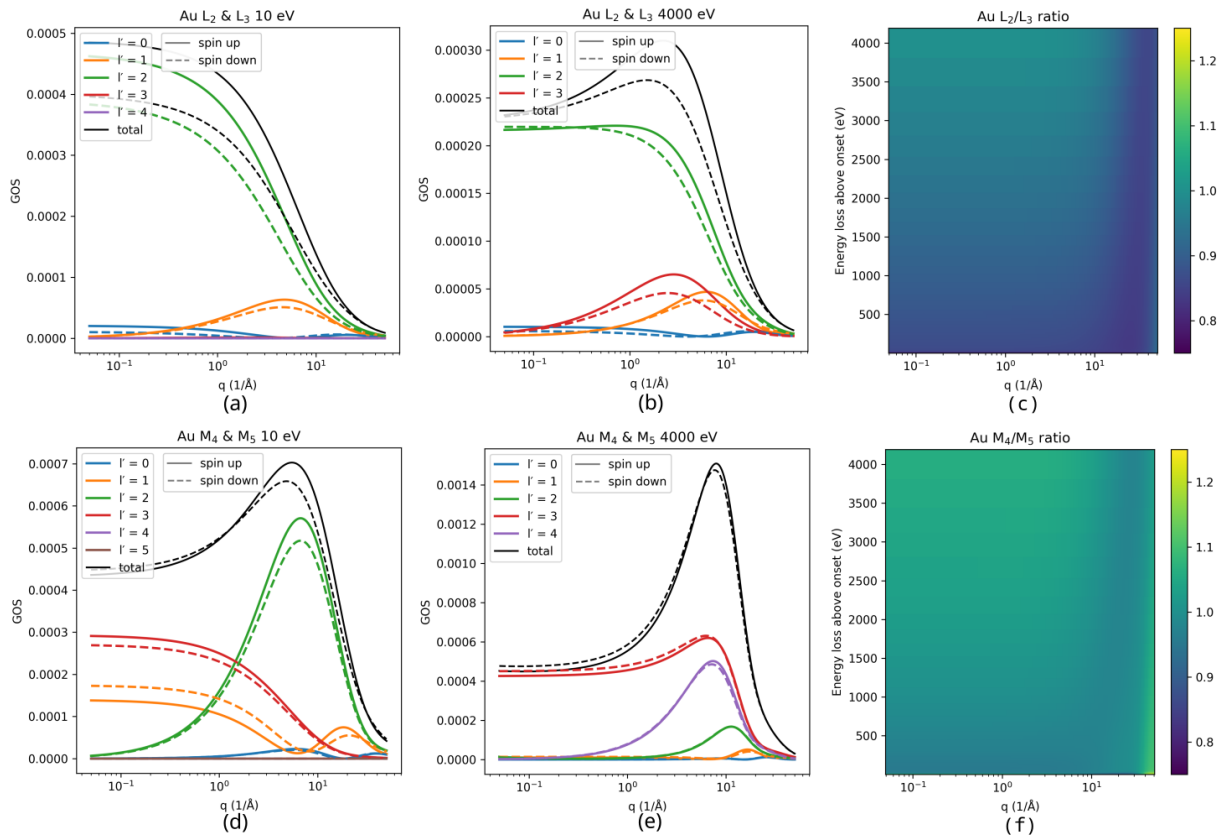


Figure 5: The decomposition of the contributions from different final states for the Au L<sub>2</sub> and L<sub>3</sub> case at (a) 10 eV and (b) 4000 eV above the ionization energy and similarly for the Au M<sub>4</sub> and M<sub>5</sub> case in (d-e). The spin-down/up GOS ratio against the energy loss and momentum transfer for (c) L<sub>2</sub>/L<sub>3</sub> and (f) M<sub>4</sub>/M<sub>5</sub> edges.

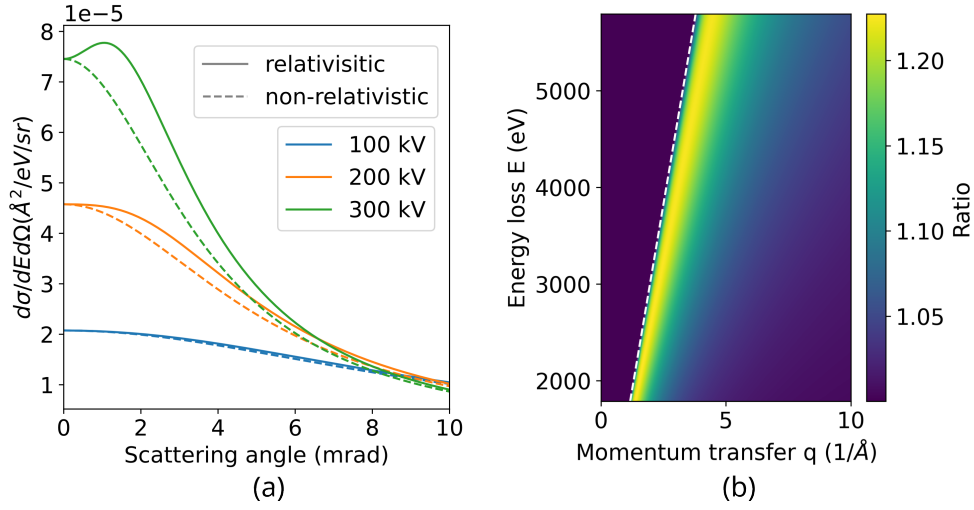


Figure 6: (a) Relativistic and non-relativistic double differential cross sections for silicon K-ionization at 10 eV above the ionization energy with the incident electron of 100 - 300 keV. (b) The ratio of relativistic to non-relativistic differential double differential cross sections for silicon K-ionization at 300 keV incident beam energy as a function of momentum transfer and energy loss. The white dashed line indicates the minimum momentum transfer.

charge in Eq. 37-38. It also leads to the interference of the longitudinal and transverse components of the excitation, resulting in anisotropic differential cross-sections which is critical when measuring near-edge fine structures [55]. Fig. 6(b) shows the ratio of relativistic to non-relativistic differential cross sections for silicon K-ionization at 300 keV incident beam energy as a function of momentum transfer and energy loss, in contrast to the single energy loss in Fig. 6(a), which agrees with previous results [54, 56]. The correction is significant at the small scattering angles and varies slowly against increasing energy loss. A white dashed line in Fig. 6(b) indicates the minimum momentum transfer. To appreciate this effect on the spectra under conventional experimental conditions, we can integrate DDSCS the scattering within the EELS collection aperture via Eq. 44 to differential scattering cross-section. To check we have the correct implementation of the relativistic correction, Fig. 7 plots the relativistic correction ratio of the Si K-edge at different

acceleration voltages with (a) 10 mrad and (b) 100 mrad collection angles using numerical calculation in Eq. 38 and analytical expression with dipole approximation in Eq. 42. The numerical calculation of the relativistic correction ratio is consistent with the analytical dipole solution in Eq. 42 for small angles of 10 mrad, yielding up to a 15% increase in the cross-sections at 300 keV. However, with increasing collection angle, the relativistic double differential cross-sections are very close to the non-relativistic ones (i.e. only about 5% for 300 keV and 100 mrad) as shown in Fig. 6. It is important to note that the dipole approximation is expected to fail at high angles and one has to use numerical relativistic corrections. Overall, we want to emphasize that the relativistic correction is important for all elements (in contrast to the relativistic atomic orbital effects, which are only obvious for core-shell electrons of heavy elements). Since this relativistic effect varies with energy loss and momentum transfer, the elemental quantification will be affected differently for different edges under varying experimental conditions. These corrections should be routinely performed when quantifying EELS with typical TEM acceleration voltages at 200-300 keV, particularly when using a small collection aperture.

### *6.3. Comparison of the Dirac-based GOS database with others*

We compared the Dirac-based GOS with the existing GOS database used in the EELS community, including the HF solutions, and DFT solutions based on the Schrödinger equation. For a fair comparison evaluation of the GOS databases themselves, the relativistic electrodynamics effect in Sec. 6.2 is not included in this comparison. In Fig. 8, the calculated spectra for O K, Ti L<sub>2</sub>, Sr L<sub>3</sub>, La M<sub>4</sub>, Bi M<sub>5</sub>, and U O<sub>5</sub> edges using different GOS databases with 300 keV incident beam energy, parallel illumination, and a 50 mrad collection angle. Overall, these spectra exhibit simi-

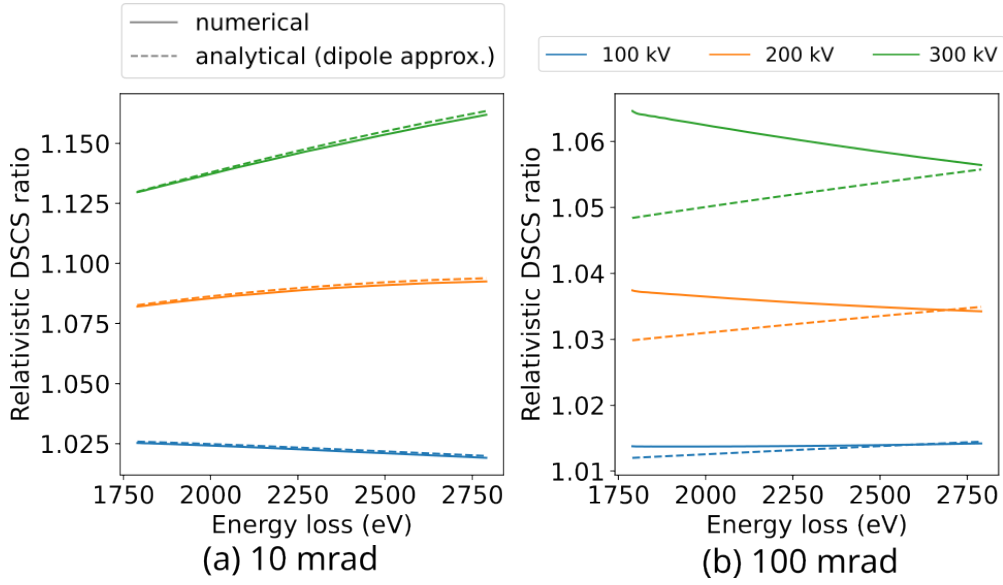


Figure 7: The relativistic differential scattering cross-section (DSCS) correction ratio of the Si K edge against the energy loss at different acceleration voltages (100-300 keV) with (a) 10 mrad and (b) 100 mrad collection angles using the full numerical solution and the analytical solution with dipole approximation.

lar shapes and absolute amplitude except for a few details. Specifically, the HF spectra are more fragmented due to the limited sampling in both energy and momentum, as shown in Fig. 1. The Schrödinger cross-sections are in good agreement with the Dirac ones for light elements where SOC is expected to be weak. However, notable differences are observed in the heavy elements for the Bi  $M_5$  and U  $O_5$  edges. Interestingly for the U  $O_5$  edge, HF and Dirac curves are in agreement while the DFT curve deviates away at the near edge region. Also, we could see a sharp peak at the start of the DFT Ti  $L_2$  edge. Since those GOS are computed using different internal numerical routines, it is difficult at this stage to pinpoint whether the discrepancy is attributed to numerical issues or the underlying physics. It could be useful to calculate the Schrödinger and Dirac solutions and construct the GOS under the same protocols to trace the causes. We noticed that there are packages (e.g. RIDIAL[66] and dftatom [73]) that can compute both the Schrödinger and Dirac

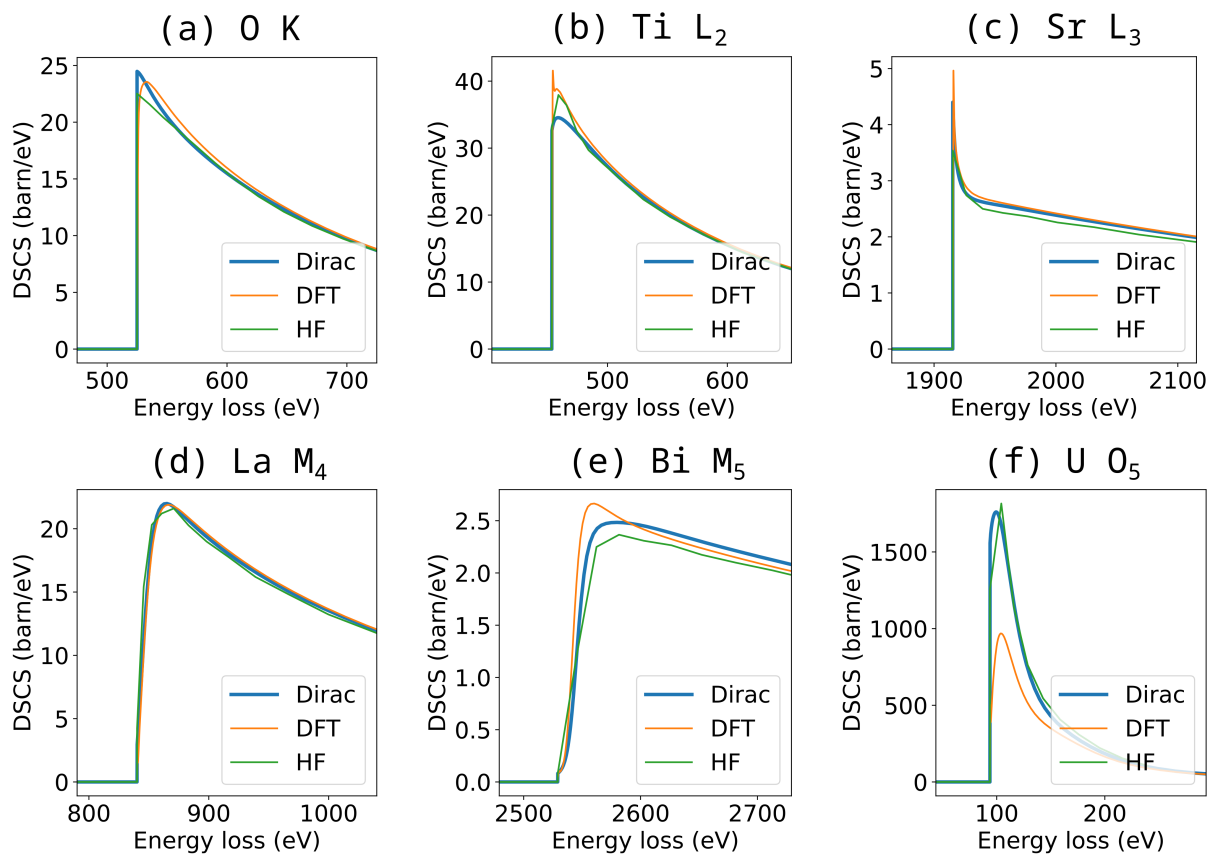


Figure 8: Comparison of the GOS databases for (a) O K, (b) Ti L<sub>2</sub>, (c) Sr L<sub>3</sub>, (d) La M<sub>4</sub>, (e) Bi M<sub>5</sub> and (f) U O<sub>5</sub> edges using different GOS databases with 300 keV incident beam, parallel illumination, and 50 mrad collection angle.



atomic radial wavefunctions, which will enable the direct comparisons.

We expect that the inner core-shell edges (i.e. K and L-edge) of heavy elements will offer a better opportunity to observe the relativistic effects, although this corresponds to extremely high energy loss that is typically not explored often in EELS. With the development of direct electron cameras and advanced spectrometers, experimental verification of the Dirac cross-sections can be expected in the future.

#### *6.4. Use of the Dirac-based GOS database*

The Dirac-based GOS database is made available open-source on Zenodo under a CC-BY license [74]. Similar to using all GOS databases, quantifying the EELS cross-sections involves a three-step process. Step 1, we need to compute the DDSCS from the GOS database given in Eq. 15 for the non-relativistic scattering but with atomic orbitals obtained from the Dirac equation. Then we use Eq. 38 to account for the relativistic nature of the fast incoming electron. Step 2, we need to integrate the DDSCS within the EELS collection aperture to obtain the differential cross-sections in Eq. 44 for parallel illumination. If convergent beam illumination is used in STEM-EELS, we have to correct it with a geometric cross-correlation function in Eq. 49 [67]. The momentum space integration for both parallel and convergent beam illumination is implemented in pyEELSModel. Step 3, the computed differential cross-sections for all edges are fitted together to the experimental spectrum for quantification. During the model-based fitting process, the core-loss spectrum can be convoluted with the low-loss spectrum to consider the source energy dispersion and plural plasmon scattering. The fitting procedure can be performed using the existing packages such as EELSModel, HyperSpy, or Gatan Digital Micrograph, which now all support the Dirac-based

GOS. We also provide a Jupyter notebook [75] to demonstrate the fitting process of the Dirac-based GOS for the Ti  $L_2/L_3$  and O K edges in  $\text{SrTiO}_3$  using `pyEELSModel` [13]. We encourage inquiries from the community and industry to integrate the Dirac-based GOS into their software packages.

## 7. Conclusions and outlook

EELS is a powerful technique for the characterization of materials composition and electronic structures. The accuracy of the EELS quantification relies on the precise calculation of the cross-sections facilitated by the GOS database, which computes the transition probability as a function of energy loss and momentum transfer. In this study, we developed an open-source Dirac-based GOS database for all elements and shells for large energy and momentum space with fine sampling. Unlike previous GOS databases relying on the Schrödinger equation, the Dirac-based GOS database better captures the relativistic effects. We demonstrated that the ionization energies calculated from the Dirac equation align well with the experimental measurements with a relative error of  $0.2\% \pm 7\%$ , including the energy splitting caused by SOC. Notably, the large component of the Dirac radial wave is shown to be equivalent to the non-relativistic Schrödinger solution at low energies, while the small component of the Dirac solution becomes significant for the core-shell electrons of heavy elements. We also showed that SOC leads to different wavefunctions and hence different transition matrix elements and GOS for spin variations. We compared the Dirac-based GOS database with existing GOS databases commonly used in the EELS community. Despite fine differences usually at the near-edge region, these spectra are generally similar for the K and L edges of light elements or the higher edges of heavy elements. But for the core-shell electrons of

heavy elements, theoretical results suggest considerable difference for spin up/down (up to 20% for Au and 40% for Ac), which is rarely measured experimentally by EELS. Further experimental work is needed to verify the Dirac-based GOS for absolute cross-sections of the heavy elements at high energy loss, which requires an advanced EELS spectrometer and detector capable of this precise measurement. Overall, the Dirac-based GOS database is expected to be useful for microanalysis with relativistic effects considered across the periodic table. In addition, the differential cross-sections could be also useful for the Monte Carlo simulations of electron scattering.

The calculations in this work are dedicated to the GOS database for EELS microanalysis. However, this computational framework can be easily extended to generate the oscillator strength database for XAS. As the momentum transfer is negligible for photons, the optical dipole oscillator strength is not dependent on the scattering angle. This can be obtained by substitution of the Hamiltonian in the transition matrix of Fermi's golden rule, which is the Coulombic interaction for an electron, with the position operator and the polarization vector of the X-ray beam. Indeed, EELS and XAS are often used in tandem to provide complementary information on materials. A pair of EELS GOS and XAS oscillator strength databases should be of interest to material scientists who use both techniques.

In analytical electron microscopy for microanalysis, the most common techniques are energy-dispersive X-ray spectroscopy (EDS) and EELS. The EDS collects the characteristic X-ray generated during the de-excitation of the core-shell electron, which is a physically coupled process and therefore its theoretical cross-sections are deeply related to the EELS calculations presented here. Experimentally, EDS elemental mapping is much simpler than EELS and favored by material scientists. However, accurate and precise EDS quantification is not easy, particularly at the atomic

scale, due to various theoretical and experimental challenges. We have generated the Dirac-based ionization potential database for atomic EDS calculations in the Bloch wave or multislice algorithms, which includes the relativistic effects from both the orbital and fast incident electron. The Dirac-based EDS database will be made available to the community in the future.

We notice that the ionization energy depends on the chemical environment, which is also expected to change the cross-sections as well. Thus, the calculation of the GOS for different oxidation states is currently under development. Moreover, our current analysis, limited to continuum states of individual atoms, fails to encapsulate the intricate unoccupied DOS inherent in complex, multi-atom systems, thereby neglecting the fine structures in the near-edge region. Given that the near-edge region often contains most of the signal counts against background and noise, the exclusion of physics-based fine structure from spectrum fitting represents a significant loss of information. Hence, we are strongly motivated to incorporate the unoccupied bounded states in our future generation of theoretical EELS cross-sections.

## **8. Data availability**

The database is available on Zenodo under a CC-BY license [74].

## **Acknowledgement**

The authors acknowledge financial support from the Research Foundation Flanders (FWO, Belgium) through Project No.G.0502.18N. This project has received funding from the European Research Council (ERC) under the European Union's Horizon 2020 research and innovation programme (Grant Agreement No. 770887 PICOMETRICS and No. 823717 ESTEEM3). The

authors acknowledge the computational resources from Vlaams Supercomputer Centrum (VSC) through Tier-1 project No.2023.023. ZZ acknowledges the travel funding from FWO (Grant No.V463823N) and the consultation with Dirk Van Dyck, Peter Schattschneider, Christian Dwyer, and Christian Rossouw. ZZ thanks Linfeng Zhang and Chu-ping Yu for reading the manuscript and offering helpful comments.

## References

- [1] R. F. Egerton, *Electron energy-loss spectroscopy in the electron microscope*, Springer Science & Business Media, 2011.
- [2] H. H. Rose, Historical aspects of aberration correction, *Journal of electron microscopy* 58 (3) (2009) 77–85.
- [3] O. L. Krivanek, T. C. Lovejoy, M. F. Murfitt, G. Skone, P. E. Batson, N. Dellby, Towards sub-10 meV energy resolution stem-eels, in: *Journal of Physics: Conference Series*, Vol. 522, IOP Publishing, 2014, p. 012023.
- [4] O. L. Krivanek, T. C. Lovejoy, N. Dellby, T. Aoki, R. Carpenter, P. Rez, E. Soignard, J. Zhu, P. E. Batson, M. J. Lagos, et al., Vibrational spectroscopy in the electron microscope, *Nature* 514 (7521) (2014) 209–212.
- [5] J. L. Hart, A. C. Lang, A. C. Leff, P. Longo, C. Trevor, R. D. Twisten, M. L. Taheri, Direct Detection Electron Energy-Loss Spectroscopy: A Method to Push the Limits of Resolution and Sensitivity, *Scientific Reports* 7 (1) (2017) 8243. doi:10.1038/s41598-017-07709-4.  
URL <https://www.nature.com/articles/s41598-017-07709-4>
- [6] B. Plotkin-Swing, G. J. Corbin, S. De Carlo, N. Dellby, C. Hoermann, M. V. Hoffman, T. C. Lovejoy, C. E. Meyer, A. Mittelberger, R. Pantelic, et al., Hybrid pixel direct detector for electron energy loss spectroscopy, *Ultramicroscopy* 217 (2020) 113067.
- [7] D. A. Muller, L. F. Kourkoutis, M. Murfitt, J. H. Song, H. Y. Hwang, J. Silcox, N. Dellby, O. L. Krivanek, Atomic-scale chemical imaging of composition and bonding by aberration-corrected microscopy, *Microscopy and Microanalysis* 14 (SUPPL. 2) (2008) 132–133. doi:10.1017/S1431927608087448.
- [8] J. A. Hachtel, J. Huang, I. Popovs, S. Jansone-Popova, J. K. Keum, J. Jakowski, T. C. Lovejoy, N. Dellby, O. L.

- Krivanek, J. C. Idrobo, Identification of site-specific isotopic labels by vibrational spectroscopy in the electron microscope, *Science* 363 (6426) (2019) 525–528.
- [9] R. Egerton, M. Malac, Improved background-fitting algorithms for ionization edges in electron energy-loss spectra, *Ultramicroscopy* 92 (2) (2002) 47–56.
- [10] Egerton, EELS textbook, 2011, publication Title: Electron spectroscopy for surface analysis.  
 URL [http://link.springer.com/chapter/10.1007/978-3-642-81099-2\\_6](http://link.springer.com/chapter/10.1007/978-3-642-81099-2_6)  
[http://link.springer.com/chapter/10.1007/978-3-642-81099-2\\_7B\\_7D6](http://link.springer.com/chapter/10.1007/978-3-642-81099-2_7B_7D6)
- [11] J. Verbeeck, S. Van Aert, Model based quantification of eels spectra, *Ultramicroscopy* 101 (2-4) (2004) 207–224.
- [12] R. Leapman, C. Swyt, Separation of overlapping core edges in electron energy loss spectra by multiple-least-squares fitting, *Ultramicroscopy* 26 (4) (1988) 393–403.
- [13] D. Jannis, joverbee/pyeelsmodel: v0.1.1 (Apr. 2024). doi:10.5281/zenodo.10992986.  
 URL <https://doi.org/10.5281/zenodo.10992986>
- [14] F. de la Peña, T. Ostasevicius, V. T. Fauske, P. Burdet, P. Jokubauskas, M. Nord, M. Sarahan, E. Prestat, D. N. Johnstone, J. Taillon, et al., Electron microscopy (big and small) data analysis with the open source software package hyperspy, *Microscopy and Microanalysis* 23 (S1) (2017) 214–215.
- [15] P. Cueva, R. Hovden, J. A. Mundy, H. L. Xin, D. A. Muller, Data processing for atomic resolution electron energy loss spectroscopy, *Microscopy and Microanalysis* 18 (4) (2012) 667–675.
- [16] W. Van den Broek, D. Jannis, J. Verbeeck, Convexity constraints on linear background models for electron energy-loss spectra, *Ultramicroscopy* 254 (2023) 113830.
- [17] J. Verbeeck, G. Bertoni, Model-based quantification of EELS spectra: Treating the effect of correlated noise, *Ultramicroscopy* 108 (2) (2008) 74–83. doi:10.1016/j.ultramic.2007.03.004.
- [18] J. Verbeeck, S. Van Aert, G. Bertoni, Model-based quantification of EELS spectra: Including the fine structure, *Ultramicroscopy* 106 (11-12 SPEC. ISS.) (2006) 976–980. doi:10.1016/j.ultramic.2006.05.006.
- [19] P. Schattschneider, *Fundamentals of inelastic electron scattering*, Springer Science & Business Media, 1986.
- [20] P. A. M. Dirac, The quantum theory of the emission and absorption of radiation, *Proceedings of the Royal Society of London. Series A, Containing Papers of a Mathematical and Physical Character* 114 (767) (1927)

243–265.

- [21] P. A. M. Dirac, The quantum theory of the electron, Proceedings of the Royal Society of London. Series A, Containing Papers of a Mathematical and Physical Character 117 (778) (1928) 610–624.
- [22] E. Fermi, Nuclear physics: a course given by Enrico Fermi at the University of Chicago, University of Chicago press, 1950.
- [23] H. Bethe, Bremsformel für elektronen relativistischer geschwindigkeit, Zeitschrift für Physik 76 (5-6) (1932) 293–299.
- [24] B. L. Moiseiwitsch, S. J. Smith, Electron impact excitation of atoms, Reviews of Modern Physics 40 (2) (1968) 238.
- [25] E. J. McGuire, Inelastic scattering of electrons and protons by the elements he to na, Physical Review A 3 (1) (1971) 267.
- [26] S. T. Manson, Inelastic Collisions of Fast Charged Particles with Atoms: Ionization of the Aluminum L Shell, Physical Review A - Atomic, Molecular, and Optical Physics 6 (3) (1972) 1013.
- [27] J. H. Scofield, K-and l-shell ionization of atoms by relativistic electrons, Physical Review A 18 (3) (1978) 963.
- [28] R. D. Leapman, P. Rez, D. F. Mayers, K, L, and M shell generalized oscillator strengths and ionization cross sections for fast electron collisions, The Journal of Chemical Physics 72 (2) (1980) 1232–1243. doi:10.1063/1.439184.
- [29] D. K. Saldin, P. Rez, The theory of the excitation of atomic inner-shells in crystals by fast electrons, Philosophical Magazine B: Physics of Condensed Matter; Statistical Mechanics, Electronic, Optical and Magnetic Properties 55 (4) (1987) 481–489. doi:10.1080/13642818708217957.
- [30] P. Rez, Inner-shell spectroscopy: An atomic view, Ultramicroscopy 28 (1-4) (1989) 16–23. doi:10.1016/0304-3991(89)90263-5.
- [31] S. Segui, M. Dingfelder, J. M. Fernández-Varea, F. Salvat, The structure of the Bethe ridge. Relativistic Born and impulse approximations, Journal of Physics B: Atomic, Molecular and Optical Physics 35 (1) (2002) 33–53. doi:10.1088/0953-4075/35/1/303.
- [32] D. Bote, F. Salvat, Calculations of inner-shell ionization by electron impact with the distorted-wave and plane-

- wave Born approximations, *Physical Review A* 77 (4) (2008) 042701. doi:10.1103/PhysRevA.77.042701.  
 URL <https://link.aps.org/doi/10.1103/PhysRevA.77.042701>
- [33] H. Kohl, H. Rose, Theory of image formation by inelastically scattered electrons in the electron microscope, in: *Advances in Electronics and Electron Physics*, Vol. 65, Elsevier, 1985, pp. 173–227.
- [34] P. Stallknecht, H. Kohl, Computation and interpretation of contrast in crystal lattice images formed by inelastically scattered electrons in a transmission electron microscope, *Ultramicroscopy* 66 (3-4) (1996) 261–275. doi:10.1016/S0304-3991(97)00007-7.
- [35] Z. L. Wang, Dynamical inelastic scattering in high-energy electron diffraction and imaging: A new theoretical approach, *Physical Review B* 41 (18) (1990) 12819. doi:10.1016/0003-4916(88)90036-8.
- [36] C. J. Rossouw, V. M. Maslen, Implications of (e, 2e) scattering for inelastic electron diffraction in crystals II. Application of the theory, *Philosophical Magazine A: Physics of Condensed Matter, Structure, Defects and Mechanical Properties* 49 (6) (1984) 743–757. doi:10.1080/01418618408236561.
- [37] D. A. Muller, J. Silcox, Delocalization in inelastic scattering, *Ultramicroscopy* 59 (1-4) (1995) 195–213. doi:10.1016/0304-3991(95)00029-Z.
- [38] E. C. Cosgriff, M. P. Oxley, L. J. Allen, S. J. Pennycook, The spatial resolution of imaging using core-loss spectroscopy in the scanning transmission electron microscope, *Ultramicroscopy* 102 (4) (2005) 317–326. doi:10.1016/j.ultramicro.2004.11.001.
- [39] L. J. Allen, A. J. D’Alfonso, S. D. Findlay, M. P. Oxley, M. Bosman, V. J. Keast, E. C. Cosgriff, G. Behan, P. D. Nellist, A. I. Kirkland, Theoretical interpretation of electron energy-loss spectroscopic images, *AIP Conference Proceedings* 999 (2008) (2008) 32–46, ISBN: 9780735405196. doi:10.1063/1.2918115.
- [40] M. P. Oxley, S. J. Pennycook, Image simulation for electron energy loss spectroscopy, *Micron* 39 (6) (2008) 676–684. doi:10.1016/j.micron.2007.10.020.
- [41] A. J. D’Alfonso, S. D. Findlay, M. P. Oxley, L. J. Allen, Volcano structure in atomic resolution core-loss images, *Ultramicroscopy* 108 (7) (2008) 677–687. doi:10.1016/j.ultramicro.2007.10.011.
- [42] J. Rusz, J. Spiegelberg, S. Muto, T. Thersleff, M. Ohtsuka, K. Leifer, P. M. Oppeneer, Localization of magnetic circular dichroic spectra in transmission electron microscopy experiments with atomic plane resolution, *Physical*



- Review B 95 (17) (2017) 1–12. doi:10.1103/PhysRevB.95.174412.
- [43] H. Yoshioka, Effect of Inelastic Waves on Electron Diffraction, *Journal of the Physical Society of Japan* 12 (6) (1957) 618–628. doi:10.1143/JPSJ.12.618.
- [44] V. W. Maslen, C. J. Rossouw, The inelastic scattering matrix element and its application to electron energy loss spectroscopy, *Philosophical Magazine A: Physics of Condensed Matter, Structure, Defects and Mechanical Properties* 47 (1) (1983) 119–130. doi:10.1080/01418618308243112.
- [45] V. W. Maslkn, C. J. Rossouw, Implications of (e, 2e) scattering for inelastic electron diffraction in crystals I. Theoretical, *Philosophical Magazine A: Physics of Condensed Matter, Structure, Defects and Mechanical Properties* 49 (6) (1984) 735–742. doi:10.1080/01418618408236560.
- [46] L. J. Allen, S. D. Findlay, M. P. Oxley, C. J. Rossouw, Lattice-resolution contrast from a focused coherent electron probe. Part I, *Ultramicroscopy* 96 (1) (2003) 47–63. doi:10.1016/S0304-3991(02)00380-7.
- [47] C. Dwyer, Multislice theory of fast electron scattering incorporating atomic inner-shell ionization, *Ultramicroscopy* 104 (2) (2005) 141–151. doi:10.1016/j.ultramic.2005.03.005.
- [48] C. Dwyer, S. D. Findlay, L. J. Allen, Multiple elastic scattering of core-loss electrons in atomic resolution imaging, *Physical Review B - Condensed Matter and Materials Physics* 77 (18) (2008) 1–8. doi:10.1103/PhysRevB.77.184107.
- [49] I. Lobato, S. van Aert, J. Verbeeck, Progress and new advances in simulating electron microscopy datasets using MULTEM, *Ultramicroscopy* 168 (2016) (2016) 17–27, publisher: Elsevier. doi:10.1016/j.ultramic.2016.06.003.  
URL <http://dx.doi.org/10.1016/j.ultramic.2016.06.003>
- [50] S. Majert, H. Kohl, Simulation of atomically resolved elemental maps with a multislice algorithm for relativistic electrons, in: *Advances in Imaging and Electron Physics*, Vol. 211, Elsevier, 2019, pp. 1–120. doi:10.1016/bs.aiep.2019.04.001.  
URL <https://linkinghub.elsevier.com/retrieve/pii/S1076567019300266>
- [51] H. G. Brown, J. Ciston, C. Ophus, Linear-scaling algorithm for rapid computation of inelastic transitions in the presence of multiple electron scattering, *Physical Review Research* 1 (3) (2019) 33186, arXiv: 1908.07628

- Publisher: American Physical Society. doi:10.1103/physrevresearch.1.033186.
- URL <https://doi.org/10.1103/PhysRevResearch.1.033186>
- [52] U. Fano, Differential Inelastic Scattering of Relativistic Charged Particles, *Physical Review* 102 (2) (1956) 385–387. doi:10.1103/PhysRev.102.385.
- URL <https://link.aps.org/doi/10.1103/PhysRev.102.385>
- [53] H. Kurata, P. Wahlbring, S. Isoda, T. Kobayashi, Importance of relativistic effect on inelastic scattering cross-sections for quantitative microanalysis, *Micron* 28 (5) (1997) 381–388. doi:10.1016/S0968-4328(97)00044-9.
- URL <https://linkinghub.elsevier.com/retrieve/pii/S0968432897000449>
- [54] R. Knippelmeyer, P. Wahlbring, H. Kohl, Relativistic ionisation cross sections for use in microanalysis, *Ultra-microscopy* 68 (1) (1997) 25–41.
- [55] P. Schattschneider, C. Hébert, H. Franco, B. Jouffrey, Anisotropic relativistic cross sections for inelastic electron scattering, and the magic angle, *Physical Review B - Condensed Matter and Materials Physics* 72 (4) (2005). doi:10.1103/PhysRevB.72.045142.
- [56] C. Dwyer, J. S. Barnard, Relativistic effects in core-loss electron diffraction, *Physical Review B - Condensed Matter and Materials Physics* 74 (6) (2006) 28–32. doi:10.1103/PhysRevB.74.064106.
- [57] K. Jorissen, J. Rehr, J. Verbeeck, Multiple scattering calculations of relativistic electron energy loss spectra, *Physical Review B* 81 (15) (2010) 155108.
- [58] J. J. Rehr, J. J. Kas, M. P. Prange, A. P. Sorini, Y. Takimoto, F. Vila, Ab initio theory and calculations of x-ray spectra, *Comptes Rendus Physique* 10 (6) (2009) 548–559.
- [59] L. Segger, Berechnung generalisierter Oszillatorenstärken für die Quantifizierung von EEL-Spektren, Bachelor's thesis, WWU-Münster (2019).
- [60] L. Segger, G. Guzzinati, H. Kohl, Generalised oscillator strengths for the simulation of eels spectra, with a broader coverage of high energy and minor edges (2023). doi:10.5281/zenodo.7645765.
- URL <https://doi.org/10.5281/zenodo.7645765>
- [61] D. R. Hamann, Generalized norm-conserving pseudopotentials, *Physical Review B* 40 (5) (1989) 2980.

- [62] G. Guzzina, GOSH: Generalised Oscillator Strengths in HDF5, gitLab repository (2023).  
URL <https://gitlab.com/gguzzina/gosh>
- [63] R. D. Cowan, The theory of atomic structure and spectra, University of California Press, 1981, tex.date-added: 2021-06-01 21:26:57 +0800 tex.date-modified: 2021-06-01 21:26:57 +0800.
- [64] F. W. Olver, NIST handbook of mathematical functions, Cambridge university press, 2010.  
URL "<https://dlmf.nist.gov/>"
- [65] W. Greiner, Relativistic quantum mechanics, Springer Berlin, Heidelberg, 2000.
- [66] F. Salvat, J. M. Fernández-Varea, RADIAL: A Fortran subroutine package for the solution of the radial Schrödinger and Dirac wave equations, Computer Physics Communications 240 (2019) 165–177, publisher: Elsevier B.V. doi:10.1016/j.cpc.2019.02.011.  
URL <https://doi.org/10.1016/j.cpc.2019.02.011>
- [67] H. Kohl, A simple procedure for evaluating effective scattering cross-sections in stem, Ultramicroscopy 16 (2) (1985) 265–268.
- [68] M. F. Gu, The flexible atomic code, Canadian Journal of Physics 86 (5) (2008) 675–689. doi:10.1139/P07-197.
- [69] P. E. Blöchl, C. J. Först, J. Schimpl, Projector augmented wave method: ab initio molecular dynamics with full wave functions, Bulletin of Materials Science 26 (2003) 33–41.
- [70] J. P. Perdew, K. Burke, M. Ernzerhof, Generalized Gradient Approximation Made Simple, Physical Review Letters 77 (18) (1996) 3865–3868, arXiv: 10.1016/0927-0256(96)00008 ISBN: 9780596529321. doi:10.1103/PhysRevLett.77.3865.  
URL <https://link.aps.org/doi/10.1103/PhysRevLett.77.3865>
- [71] C. C. Ahn, Transmission electron energy loss spectrometry in materials science and the EELS atlas, John Wiley & Sons, 2006.
- [72] A. Y. Lee, D. M. Blakeslee, C. J. Powell, J. R. Rumble Jr, Development of the web-based nist x-ray photoelectron spectroscopy (xps) database, Data Science Journal 1 (2002) 1–12.
- [73] O. Čertík, J. E. Pask, J. Vackář, dftatom: A robust and general schrödinger and dirac solver for atomic structure

calculations, *Computer Physics Communications* 184 (7) (2013) 1777–1791.

[74] Z. Zhang, I. Lobato, D. Jannis, J. Verbeeck, S. Van Aert, P. Nellist, Generalised oscillator strength for core-shell electron excitation by fast electrons based on dirac solutions (2024). doi : 10.5281/zenodo.11199911.

URL <https://doi.org/10.5281/zenodo.11199911>

[75] Z. Zhang, Gos demo: Tutorial on how to use dirac gos for eels quantification (2024).

URL [https://github.com/zezhong-zhang/gos\\_demo](https://github.com/zezhong-zhang/gos_demo)